

Kinetic Energy Exchanges between a Two-Dimensional Front and Internal Waves[©]

SUBHAJIT KAR^a AND ROY BARKAN^{a,b}

^a Porter School of the Environment and Earth Sciences, Tel Aviv University, Ramat Aviv, Israel

^b Department of Atmospheric and Oceanic Sciences, University of California, Los Angeles, Los Angeles, California

(Manuscript received 22 November 2022, in final form 13 July 2023, accepted 18 July 2023)

ABSTRACT: Fronts and near-inertial waves (NIWs) are energetic motions in the upper ocean that have been shown to interact and provide a route for kinetic energy (KE) dissipation of balanced oceanic flows. In this paper, we study these KE exchanges using an idealized model consisting of a two-dimensional geostrophically balanced front undergoing strain-induced semigeostrophic frontogenesis and internal wave (IW) vertical modes. The front-IW KE exchanges are quantified separately during two frontogenetic stages: an exponential sharpening stage that is characterized by a low Rossby number and is driven by the imposed strain (i.e., mesoscale frontogenesis), followed by a superexponential sharpening stage that is characterized by an $\mathcal{O}(1)$ Rossby number and is driven by the convergence of the secondary circulation (i.e., submesoscale frontogenesis). It is demonstrated that high-frequency IWs quickly escape the frontal zone and are very efficient at extracting KE from the imposed geostrophic strain field through the deformation shear production (DSP). Part of the extracted KE is then converted to wave potential energy. On the contrary, NIWs remain locked to the frontal zone and readily exchange energy with the ageostrophic frontal circulation. During the exponential stage, NIWs extract KE from the geostrophic strain through DSP and transfer it to the frontal secondary circulation via the ageostrophic shear production (AGSP) mechanism. During the superexponential stage, a newly identified mechanism, convergence production (CP), plays an important role in the NIW KE budget. The CP transfers KE from the convergent ageostrophic secondary circulation to the NIWs and largely cancels out the KE loss due to the AGSP. This CP may explain previous findings of KE transfer enhancement from balanced motions to IWs in frontal regions of realistic ocean models. We provide analytical estimates for the aforementioned energy exchange mechanisms that match well the numerical results. This highlights that the strength of the exchanges strongly depends on the frontal Rossby and Richardson numbers.

SIGNIFICANCE STATEMENT: Fronts with large horizontal density and velocity gradients are ubiquitous in the upper ocean. They are generated by a process known as frontogenesis, which is often initialized by straining motions of mesoscale balanced circulations. Here we examine the energy exchanges between fronts and internal waves in an idealized configuration, aiming to elucidate the mechanisms that can drain energy from oceanic balanced circulations. We identify a new mechanism for energy transfers from the frontal circulation to near-inertial internal waves called convergence production. This mechanism is especially effective during the later stages of frontogenesis when the convergent ageostrophic secondary circulation that develops is strong.

KEYWORDS: Convergence/divergence; Frontogenesis/frontolysis; Fronts; Internal waves; Secondary circulation

1. Introduction

Mesoscale geostrophic eddies comprise the largest reservoir of kinetic energy (KE) in the ocean (Ferrari and Wunsch 2009). Because their dynamics are constrained by geostrophic and hydrostatic balances, they are expected, according to geostrophic turbulence theory (Salmon 1980), to transfer their KE to larger scales (inverse cascade). The mechanisms that halt that inverse KE cascade, and permit a forward KE cascade to dissipative scale, have been a topic of much debate in oceanography (Müller et al. 2005).

We focus here on the mechanism first proposed by Gertz and Straub (2009), whereby storm-forced near-inertial waves (NIWs) can interact with mesoscale geostrophic eddies and

drain a considerable fraction of their KE. To explain this mechanism, Xie and Vanneste (2015) constructed an asymptotic theory based on the generalized Lagrangian-mean framework (GLM) to study the interactions between NIWs and balanced quasigeostrophic (QG) flow. Wagner and Young (2016) arrived at a similar NIW–QG coupled system by using an Eulerian-based multiple time scale approach. In both theories the NIW dynamics is governed by the so-called YBJ equation (Young and Ben Jelloul 1997).¹ The essential ingredients in these reduced models are the conservation of the total energy (QG + NIW) and the near-inertial wave action (or wave kinetic energy). Rocha et al. (2018) studied the NIW–QG system in coupled numerical simulations of barotropic (2D) turbulence and NIW vertical modes. They demonstrated that any reduction in the horizontal scales of NIWs must be accompanied by an increase in wave potential energy and a subsequent reduction in the kinetic energy of the balanced flow (a mechanism they referred to as “stimulated

[©] Supplemental information related to this paper is available at the Journals Online website: <https://doi.org/10.1175/JPO-D-22-0240.s1>.

Corresponding author: Subhajit Kar, subhajitkar@mail.tau.ac.il

¹ Later refined to the YBJ⁺ equation (Asselin and Young 2019).

generation”). It is noteworthy, however, that stimulated generation is only cleanly identified in the GLM framework where the Lagrangian-mean balanced flow contains wave-induced contributions. It remains difficult to evaluate stimulated generation in Eulerian-based numerical models or in situ measurements.

[Thomas and Arun \(2020\)](#) and [Thomas and Daniel \(2021\)](#) used idealized numerical simulations of Boussinesq flow in the small Rossby number parameter regime, characteristic of QG dynamics, and showed that when the wave amplitude is much larger than that of the QG flow (i.e., strong-wave limit), NIWs can exchange energy with the balanced flow, thereby facilitating a downscale KE cascade. It was further demonstrated that when the wave and balanced flow amplitudes are comparable, the downscale cascade is reduced and results in the accumulation of KE at large scales. Using numerical simulations of the NIW–QG reduced model, [Xie \(2020\)](#) demonstrated that NIWs can catalyze a downscale energy flux of the balanced mean-flow energy without a direct energy exchange, unlike the model of [Thomas and Daniel \(2021\)](#).

Other numerical studies have examined more realistic configurations and investigated the balanced flow evolution under the influence of high-frequency wind forcing. For example, [Taylor and Straub \(2016\)](#) simulated an eddy-permitting wind-driven channel flow and showed that the Reynolds stresses associated with NIWs can provide a route for KE dissipation of mesoscale geostrophic flow. [Barkan et al. \(2017\)](#) used a similar configuration albeit with a much higher spatial resolution that allowed to simulate submesoscale currents, which are characterized by a much larger Rossby number ([Thomas et al. 2008; McWilliams 2016](#)). They demonstrated that the internal wave-induced energy pathways include two routes—first, direct energy extraction from the mesoscale flow by the externally forced NIWs followed by an internal wave downscale KE cascade to dissipation, and second, a stimulated imbalance process that involves an IW triggered forward energy cascade from meso to submeso time scales.

The effects of strongly baroclinic fronts on the polarization relations of NIWs and the subsequent energy exchanges were studied by [Thomas \(2012\)](#). [Thomas \(2012\)](#) developed an idealized model for an unbounded two-dimensional front and showed that NIWs efficiently extract energy from a geostrophic deformation field and transfer it to the ageostrophic circulation that develops spontaneously during frontogenesis. [Whitt and Thomas \(2015\)](#) used a slab mixed layer model to illustrate that inertial oscillations can exchange energy periodically with a unidirectional, laterally sheared geostrophic flow, and [Jing et al. \(2017\)](#) pointed out that it is the geostrophic strain that makes this energy transfer permanent.

The motivation for the present work stems from the study of IW and eddy interactions in [Barkan et al. \(2021\)](#), who analyzed realistic, nested, high-resolution simulations in the North Atlantic Subpolar Gyre that included both NIWs and internal tides. The authors demonstrated that wind forced NIWs triggered a substantial transfer of KE from sub- to superinertial time scales, which was spatially localized in strongly baroclinic frontal regions that are characterized by high positive Rossby numbers and strong horizontal convergence ([Fig. 1](#)). This

strong departure from geostrophic balance is generic for surface-intensified submesoscale fronts and filaments that are prevalent during winter months ([Capet et al. 2008; D'Asaro et al. 2018](#)) and that cannot be adequately described by QG dynamics ([McWilliams 2016](#)). To gain mechanistic understanding of these energy exchanges, we developed an idealized model consisting of a two-dimensional front undergoing strain-induced semigeostrophic frontogenesis ([Hoskins and Bretherton 1972](#), hereinafter **HB72**) and IW vertical modes. In the **HB72** model, the frontal sharpening process occurs in two stages—an “exponential” growth stage, driven by the imposed geostrophic deformation field, followed by a “superexponential” growth stage, driven by the horizontally convergent ageostrophic secondary circulation (ASC). This superexponential growth stage is characteristic of the oceanic submesoscale frontogenesis that we aim to model (e.g., [Barkan et al. 2019](#)). Recently, [Srinivasan et al. \(2022\)](#) showed that the horizontally convergent ASC that drives submesoscale frontogenesis leads to a forward energy cascade. Here, we demonstrate that the same horizontally convergent ASC allows NIWs to extract KE efficiently from the frontal circulations. Like [Srinivasan et al. \(2022\)](#), we refer to this new IW–submesoscale exchange mechanism as convergence production (CP). The CP is shown here to be the dominant KE extraction mechanism by all NIW modes considered during the superexponential frontogenesis stage.

The paper is organized as follows: in [sections 2](#) and [3](#) we discuss the configuration used to study front–IW interactions, distinguishing between minimum frequency (near-inertial) and high-frequency IWs. The details of the numerical setup are provided in [section 4](#), and in [section 5](#) we discuss the evolution of the mean flow. A detailed analysis of the front–IW energy exchanges is shown in [section 6](#). Finally, in [section 7](#), we summarize our findings and draw connections to realistic ocean scenarios.

2. Problem configuration

An idealized configuration is developed to study front–IW energy exchanges. The configuration consists of a 2D (i.e., invariant in the x direction) geostrophically balanced front undergoing strain-induced frontogenesis in a vertically bounded domain of depth H , to which we add IW vertical modes. The domain is periodic in the horizontal direction with width L . The model assumes a time-scale separation between the mean flow and IWs, where the mean-flow evolution is governed by the **HB72** uniform potential vorticity (PV) frontogenesis model. The dynamics of the linear IW vertical modes are governed by the hydrostatic, Boussinesq equations of motion for a rotating fluid under the f -plane approximation.

a. Uniform PV **HB72** model

The mean-flow velocity [$\bar{\mathbf{U}} = (\bar{U}, \bar{V}, \bar{W})$], buoyancy (\bar{B}), and pressure (\bar{P}) fields in the **HB72** model take the form

$$\bar{U} = \alpha x + U(y, z, t), \quad (1a)$$

$$\bar{V} = -\alpha y + V(y, z, t), \quad (1b)$$

$$\bar{W} = W(y, z, t), \quad (1c)$$

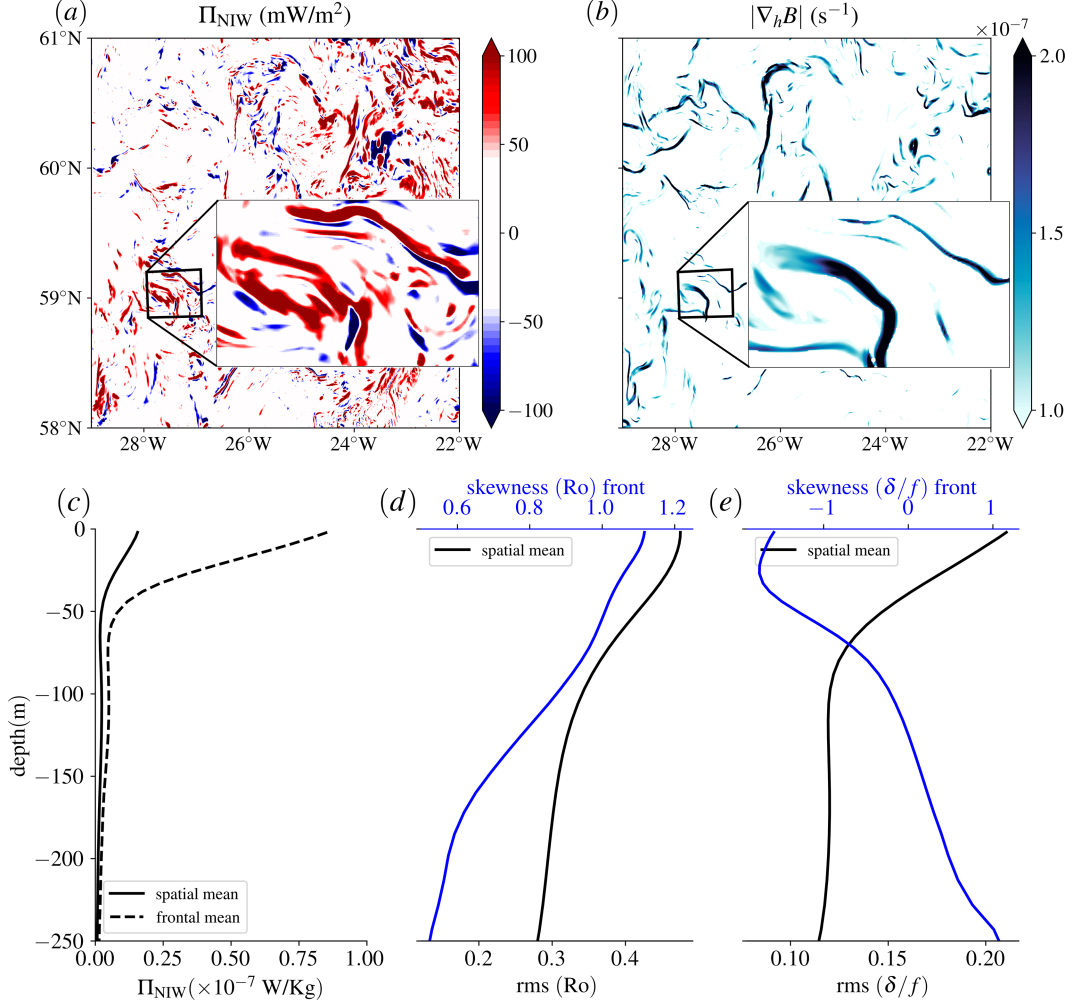


FIG. 1. Interactions between IWs and submesoscale fronts and filaments in realistic simulations of the North Atlantic Subpolar Gyre region during winter (adapted from Barkan et al. 2021). Representative snapshots of (a) the mixed layer integrated KE energy transfers from sub- to superinertial time scales (indicated by positive Π_{NIW} values) computed using the coarse-graining approach (Eyink 2005), and (b) the 90th percentile of subinertial horizontal buoyancy gradient magnitudes $|\nabla_h B|$, representing submesoscale frontal regions. Insets in (a) and (b) illustrate how flow structures with strong positive KE transfers from sub- to superinertial motions are collocated with submesoscale frontal regions. (c) Time mean sub- to superinertial KE transfers, averaged separately over the entire domain (solid black line) and over frontal regions (dashed black line), demonstrate that the strongest interactions are found at submesoscale structures. The time-mean, frontal averaged, root-mean-square (rms) of (d) the Rossby number, Ro , (defined as the vertical vorticity ζ normalized by the local Coriolis frequency f ; solid black line) and (e) horizontal divergence normalized by the Coriolis frequency [rms(δ/f); solid black line] show the significant ageostrophic frontal circulations that are dominated by cyclonic and convergent motions [positive Ro skewness and negative δ/f skewness; solid blue lines].

$$\bar{P} = P_0(x, y) + P(y, z, t), \quad (1d)$$

$$\bar{B} = B(y, z, t), \quad (1e)$$

where α denotes a spatially and temporally uniform large-scale geostrophic strain, which is used to initiate frontogenesis, and the velocity components \bar{U} , \bar{V} , and \bar{W} are oriented in the \hat{x} , \hat{y} , and \hat{z} directions, respectively. The mean-flow pressure \bar{P} consists of a pressure field that balances the geostrophic deformation flow $P_0 = -\rho_0[\alpha^2(x^2 + y^2)/2 + f\alpha xy]$ and P , which is in

hydrostatic balance with the mean-flow buoyancy $B = -gp'/\rho_0$ (p' is the mean-flow density perturbation relative to the reference density ρ_0 , and g is the gravitational acceleration).

In semigeostrophic theory the alongfront velocity U is purely geostrophic

$$U = U_g = -\frac{1}{f} \frac{\partial P}{\partial y}, \quad (2)$$

and the buoyancy field B is related to U_g via the thermal-wind balance,

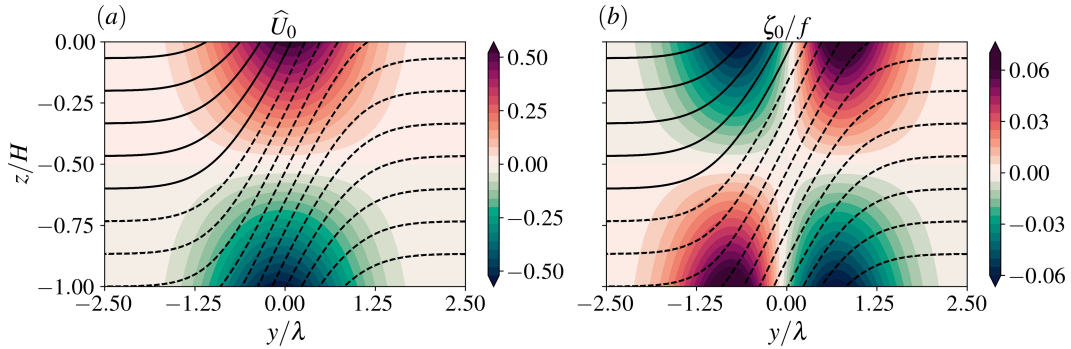


FIG. 2. The initial condition of (a) the alongfront velocity $\hat{U}_0(y, z) = \hat{U}(y, z, 0)$ [Eq. (9a)] and (b) vertical vorticity $\zeta_0 [= -\partial_y U(y, z, 0)]$ normalized by the Coriolis frequency f . Contour lines of the initial buoyancy field \hat{B} [Eq. (9c)] are displayed with a 0.22 contour interval (the solid and dotted lines show positive and negative values, respectively).

$$\frac{\partial U_g}{\partial z} = \frac{S^2}{f}, \quad (3)$$

where $S^2 \equiv -\partial B/\partial y$. The associated hydrostatic PV, q , is defined as

$$q(y, z, t) = (f\hat{z} + \nabla \times \mathbf{U}) \cdot \nabla B. \quad (4)$$

In this study we follow the formulation of [Shakespeare and Taylor \(2013\)](#) to solve the [HB72](#) model, using the generalized momentum coordinates

$$Y = e^{\alpha t} \left(y - \frac{U}{f} \right), \quad (5a)$$

$$Z = z, \quad (5b)$$

$$T = t. \quad (5c)$$

For a mean flow with uniform PV, the associated buoyancy field can generally be defined as

$$B(Y, Z, T) = N^2 Z + B_0(Y) + \Delta B(Y, Z, T), \quad (6)$$

where $B_0(Y)$ represents an imposed initial buoyancy distribution, which we pick to be

$$B_0(Y) = \mathcal{B} \operatorname{erf}(Y/\lambda), \quad (7)$$

where λ is the cross-frontal length scale. This initial buoyancy distribution describes a localized frontal zone with characteristics horizontal buoyancy gradient $S^2 = \mathcal{B}/\lambda$. In [appendix A](#) we show that ΔB represents the buoyancy anomaly required to satisfy the uniform PV ansatz [Eq. (A4b)], and that the evolution equation for semigeostrophic frontogenesis is given by

$$\left(f^2 \frac{\partial^2}{\partial Z^2} + N^2 e^{2\alpha T} \frac{\partial^2}{\partial Y^2} \right) \Phi = -f e^{\alpha T} \frac{dB_0}{dY}, \quad (8)$$

where $\Phi(Y, Z, T) = \int_{-H}^Z U(Y, Z', T) dZ'$. We assume top and bottom rigid lid boundary conditions and that all fields decay to zero away from the frontal zone (e.g., as $y \rightarrow \pm\infty$). The

above equation can be solved using a Fourier transform in Y and sine transform in Z (to satisfy the rigid lid conditions), given a prescribed initial buoyancy field $B_0(Y)$ [e.g., Eq. (7)]. Once the solution of Φ is known, the solutions of alongfront velocity $U(Y, Z, T)$, flow buoyancy $B(Y, Z, T)$ and ASC streamfunction Ψ are obtained by using Eqs. (A14)–(A16), respectively. To facilitate the connection between our model solutions and realistic oceanic flows we nondimensionalize mean-flow variables U, V, B , and Ψ using

$$\hat{U} = \frac{1}{|S^2|H/f} U, \quad (9a)$$

$$\hat{V} = \frac{2\alpha}{f} \hat{U}, \quad (9b)$$

$$\hat{B} = \frac{B}{|S^2|\lambda}, \quad (9c)$$

$$\hat{\Psi} = \frac{2\alpha}{f} \hat{U} H, \quad (9d)$$

where the scaling for the cross-front ageostrophic velocity \hat{V} follows the semigeostrophic frontogenesis scaling of [HB72](#). The initial alongfront geostrophic velocity \hat{U} and the initial Rossby number, Ro , (defined as the initial vertical vorticity ζ_0 normalized by Coriolis frequency) are shown in [Fig. 2](#). The initial Rossby and Richardson numbers are set to be small and large, respectively, to mimic an oceanic mesoscale frontal zone ([Table 1](#)).

b. Internal wave evolution equations and initial conditions

The evolution equations for the IW velocity [$\mathbf{u} = (u, v, w)$], buoyancy (b), and pressure (p) are

$$\frac{Du}{Dt} - (1 + \text{Ro})fv + \frac{S^2}{f}w + \alpha u = 0, \quad (10a)$$

$$\frac{Dv}{Dt} + \delta v + w \frac{\partial V}{\partial z} + fu - \alpha v = -\frac{\partial p}{\partial y}, \quad (10b)$$

TABLE 1. The nondimensional parameters governing the 2D front-IW model.

Parameter	Definition	Value
	Nondimensional parameters for the front	
λ/H	Aspect ratio of the initial front	200
Ro_{rms}	Initial root-mean-square Rossby number of the front	0.03
$(\text{Ri}_g)_{\text{rms}}$	Initial root-mean-square Richardson number of the front	15
a/f	Deformation ratio	(0.04, 0.1)
	Nondimensional parameters for the NIW	
ω/f	Initial nondimensional NIW frequency	0.98
Bu	Burger number of the NIW	2.24
	Nondimensional parameters for the high-frequency IW	
ω/f	Initial nondimensional high-frequency IW	1.50
Bu	Burger number of mode-1 high-frequency IW	1.18

$$0 = -\frac{\partial p}{\partial z} + b, \quad (10c)$$

$$\frac{Db}{Dt} - S^2 v + \frac{\partial B}{\partial z} w = 0, \quad (10d)$$

$$\frac{\partial v}{\partial y} + \frac{\partial w}{\partial z} = 0, \quad (10e)$$

where the material derivative $D/Dt = \partial/\partial t + (V - \alpha y)\partial/\partial y + W\partial/\partial z$, the Rossby number Ro is defined as $\text{Ro} = -\partial_y U/f = \zeta/f$, $\delta = \partial V/\partial y$ is the horizontal divergence associated with the ASC and the thermal-wind balance [e.g., Eq. (3)] is used to derive Eq. (10a). Because we only consider linear wave dynamics, quadratic wave quantities are discarded and our model cannot capture wave-wave interactions. Furthermore, the inclusion of phase-averaged wave momentum and buoyancy fluxes in the mean-flow evolution equations (i.e., full coupling) is left for future work.

To derive the IW initial conditions, we set α to zero and exploit the fact that the initial conditions for the mean flow contain no ASC ($V_0 = W_0 = 0$), such that D/Dt can be approximated by $\partial/\partial t$. The problem configuration allows us to introduce a streamfunction χ such that

$$v = \frac{\partial \chi}{\partial z}, \quad (11a)$$

$$w = -\frac{\partial \chi}{\partial y}, \quad (11b)$$

and simplify Eqs. (10a)–(10e) to a single partial differential equation for χ (e.g., Whitt and Thomas 2013)

$$\left(f_{\text{eff}}^2 + \frac{\partial^2}{\partial t^2}\right) \frac{\partial^2 \chi}{\partial z^2} + 2S^2 \frac{\partial^2 \chi}{\partial y \partial z} + N^2 \frac{\partial^2 \chi}{\partial y^2} = 0, \quad (12)$$

where $f_{\text{eff}} = f\sqrt{1 + \text{Ro}}$ is the effective Coriolis frequency (e.g., Kunze 1985). To make progress, we assume that the variables f_{eff} and S^2 are constant, which is justified in the frontal

zonal ($-1 < y/\lambda < 1$ in Fig. 2) when the initial Rossby number is sufficiently small. Following Gerkema and Shirira (2005), we look for plane-wave solutions of the form

$$\chi(y, z) = \tilde{\chi}(z) \exp\{il(y - c_1 z)\} \exp(-i\omega t), \quad (13)$$

where $c_1 = S^2/(f_{\text{eff}}^2 - \omega^2)$ is a constant, ω is the wave frequency, and l is the wavenumber in the y direction. Substituting the above ansatz into Eq. (12) yields

$$\frac{d^2 \tilde{\chi}}{dz^2} + l^2(c_1^2 - c_0^2)\tilde{\chi} = 0, \quad (14)$$

where $c_0 = N^2/(f_{\text{eff}}^2 - \omega^2)$ is, again, assumed constant. Equation (14), subject to the boundary conditions,

$$\tilde{\chi}(z = 0) = \tilde{\chi}(z = -H) = 0 \quad (15)$$

has solutions of the form

$$\tilde{\chi}_n(z) = \mathcal{A}_n \sin(m_n z), \quad m_n = \frac{n\pi}{H}, \quad (16)$$

where m_n is the vertical wavenumber of the n th mode, and $\mathcal{A}_n \in \mathbb{R}$. The remaining fields are given by Eqs. (11a), (11b), (10a), and (10d)

$$[v, w] = [\underbrace{-ilc_1 \tilde{\chi}_n + \partial_z \tilde{\chi}_n}_{\tilde{v}}, \underbrace{-il \tilde{\chi}_n}_{\tilde{w}}] \exp\{il(y - c_1 z) - i\omega t\}, \quad (17a)$$

$$u = \frac{i}{\omega f} (f_{\text{eff}}^2 \tilde{v} - S^2 \tilde{w}) \exp\{il(y - c_1 z) - i\omega t\}, \quad (17b)$$

$$b = \frac{i}{\omega} (S^2 \tilde{v} - N^2 \tilde{w}) \exp\{il(y - c_1 z) - i\omega t\}, \quad (17c)$$

with the dispersion relation

$$\begin{aligned} \omega^2 &= f_{\text{eff}}^2 + \frac{l^2 N^2}{2m_n^2} \left(1 \pm \sqrt{1 + \frac{4m_n^2 S^4}{l^2 N^4}}\right) \\ &= f_{\text{eff}}^2 + \frac{l^2 N^2}{2m_n^2} \left(1 \pm \sqrt{1 + \frac{4}{\text{Ri}_g \text{Bu}}}\right), \end{aligned} \quad (18)$$

where the geostrophic Richardson number and IW Burger number are defined as

$$\text{Ri}_g = N^2/(\partial_z U)^2 = f^2 N^2/S^4, \quad \text{Bu} = (l^2 N^2)/(f^2 m_n^2). \quad (19)$$

For finite scale low-mode IWs in a geostrophically balanced frontal zone $\text{Bu} \sim \mathcal{O}(1)$, $\text{Ri}_g \gg 1$ and $4/(\text{Ri}_g \text{Bu}) \ll 1$ (the initial values of Ri_g , Ro , and Bu are displayed in Table 1). The expression in the squared root can thus be expanded in a Taylor series, and Eq. (18) becomes

$$\omega^2 \approx f_{\text{eff}}^2 + \frac{l^2 N^2}{2m_n^2} \left[1 \pm \left(1 + 2 \frac{m_n^2 S^4}{l^2 N^4}\right)\right]. \quad (20)$$

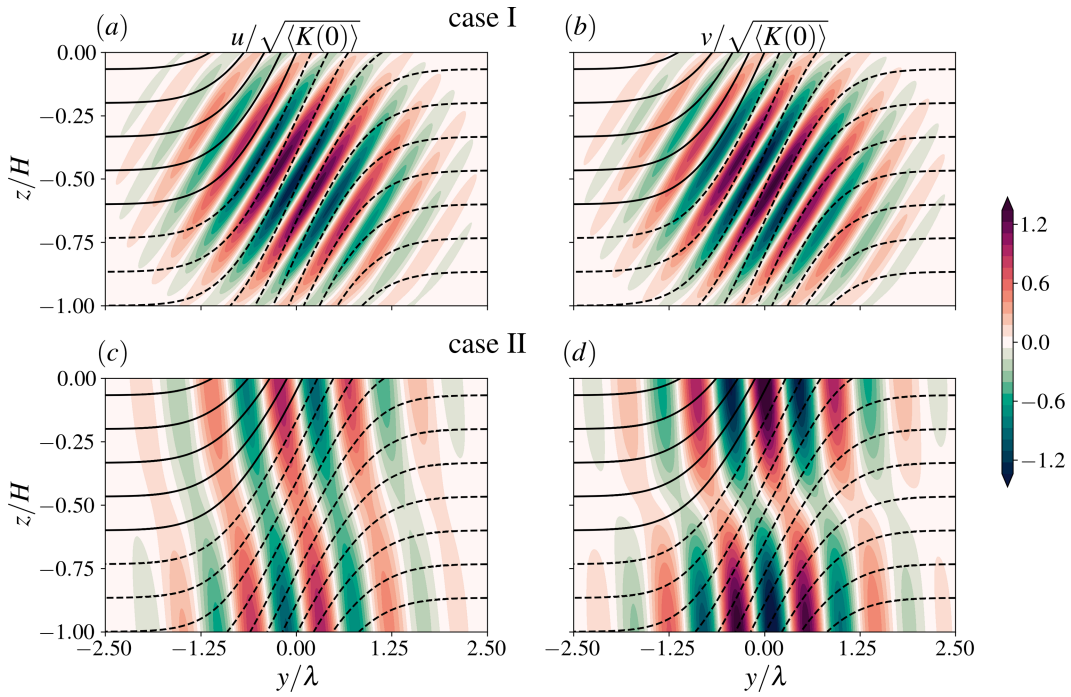


FIG. 3. Initial conditions for mode 1 (a),(c) alongfront and (b),(d) cross-front IW velocities [normalized by the square root of initial domain-averaged wave KE, $\sqrt{\langle K(0) \rangle}$]. Contour lines of the initial buoyancy field \hat{B} [Eq. (9c)] are displayed with a 0.22 contour interval (the solid and dotted lines show positive and negative values, respectively). The NIW frequency (case I, $\omega = 0.98f$) is computed from Eq. (21a) using the initial rms Ro and Ri_g values (Table 1). For the NIW, phase lines are parallel to isopycnals near the frontal zone whereas for high-frequency IW (case I, $\omega = 1.5f$) phase lines are tilted against the isopycnals near the frontal zone. Note that the “high” mode structure in case I is a result of the baroclinicity of the mean flow, not the initial conditions.

From Eq. (20) the minimum IW frequency ω_{\min} and the polarization relations are

$$\omega_{\min} \approx f \sqrt{1 + Ro - Ri_g^{-1}}, \quad (21a)$$

$$(u, v, w) \approx v \left(i \frac{\omega_{\min}}{f}, 1, \frac{S^2}{N^2} \right), \quad (21b)$$

where the smallness of $1/(Ri_g Bu)$ has been used. This recovers the expressions derived in Whitt and Thomas (2013) and shows that vorticity and baroclinicity allow the IW frequency to be lower than the inertial frequency.² The corresponding horizontal group velocity c_{g_y} takes the form

$$c_{g_y} \approx \pm \frac{N^3(\omega^2 - \omega_{\min}^2)^{3/2}}{m_n \omega [2S^4 + N^2(\omega^2 - f_{\text{eff}}^2)]}, \quad (22)$$

where the positive (negative) sign corresponds to $l > 0$ ($l < 0$).

The IW initial conditions consist of a Gaussian packet of a mode-1 IW [m_1 in Eqs. (17a)–(17c)], with a horizontal width of three wavelengths ($6\pi/l$), and with phase lines approximately

parallel to (case I: NIW) or tilted against (case II: high-frequency IW) isopycnals (Fig. 3). Evidently, our assumptions of an initially constant Ro and S^2 (or Ri_g) do not hold over the entire domain and so the NIW isophases are only approximately parallel to isopycnals in the frontal zone. Nevertheless, as will be shown in the following sections (see also Movie 1 in the online supplemental material), the IW mode in case I behaves like a minimum frequency wave because it remains phase-locked to the frontal zone [$c_{g_y} \rightarrow 0$, Eq. (22)] and is, therefore, more likely to exchange energy with the frontal circulations (Thomas 2012). On the contrary, case II corresponds to a higher-frequency IW (viz., $\omega = 1.5f$) that can propagate away from the frontal zone [$c_{g_y} \neq 0$, Eq. (22)] and is, therefore, less likely to exchange energy with the frontal flow. In section 6 we compare and contrast the two cases.

3. Internal wave energy equations

The following IW KE equation is obtained by multiplying Eq. (10a) with u and Eq. (10b) with v ,

$$\begin{aligned} \frac{\partial K}{\partial t} = & \underbrace{-\nabla \cdot (\mathbf{V}K)}_{\text{ADVEC}} + \alpha y \underbrace{\frac{\partial K}{\partial y}}_{\text{GSP}} - \underbrace{\frac{S^2}{f} uw}_{\text{LSP}} - \underbrace{f R o u v}_{\text{DSP}} - \underbrace{\alpha(u^2 - v^2)}_{\text{DWP}} \\ & - \underbrace{\delta v^2}_{\text{CP}} - \underbrace{v w \frac{\partial V}{\partial z}}_{\text{BFLUX}} + \underbrace{w b}_{\text{PWORK}} - \underbrace{\nabla \cdot \mathbf{v} p}_{\text{AGSP}} \end{aligned} \quad (23)$$

² The imposed geostrophic strain modifies the IW frequency at $\mathcal{O}[(\alpha/f)^2]$, which is negligible in our case compared with the effects of vorticity and baroclinicity (Jing et al. 2017).

where $K = 1/2(u^2 + v^2)$, $\nabla = (\partial/\partial y, \partial/\partial z)$, $\mathbf{v} = (v, w)$, $\mathbf{V} = (V, W)$. The energy exchange terms in (23) are the geostrophic shear production (GSP), denoting wave-mean-flow energy exchanges associated with the geostrophic vertical shear; the lateral shear production (LSP), denoting wave-mean-flow energy exchanges associated with the geostrophic lateral shear; the deformation shear production (DSP), denoting energy exchanges due to the imposed deformation flow; the ageostrophic shear production (AGSP), denoting wave-mean-flow energy exchanges associated with the ageostrophic vertical shear; the convergence production (CP), denoting wave-mean-flow energy exchanges associated with the lateral ageostrophic horizontally divergent motions; the buoyancy flux (BFLUX), indicating the energy exchanges between wave kinetic and potential energies; the pressure work (PWORK), denoting wave energy changes due to the propagation of pressure perturbations.

The advection term ADVEC can be expressed as

$$\text{ADVEC} = -\nabla \cdot (\mathbf{V}K) + \frac{\partial}{\partial y}(\alpha y K) - \alpha K. \quad (24)$$

The first term on the right-hand side of the Eq. (24) vanishes when averaged over the domain for our choice of boundary conditions, while the second term vanishes because in our numerical model, K is set to zero at the periodic boundaries (e.g., Fig. 3). The third term, however, is an effective energy sink due to the imposed strain in a 2D configuration. Although the energy sink magnitude is larger than that of the various exchange terms, it does not represent an energy exchange between the wave and mean flow. We verified that it does not affect the energy exchanges discussed in the manuscript by rerunning the numerical simulations with an artificial source term that compensates for the energy loss (not shown). We, therefore, focus on $\Delta\langle K_{\text{net}} \rangle(t)$, which represents solely the domain-averaged IW KE changes at time t relative to the initial time $t = 0$ due to front-IW energy exchanges. $\Delta\langle K_{\text{net}} \rangle(t)$ is defined as

$$\begin{aligned} \Delta\langle K_{\text{net}} \rangle(t) &\equiv \langle K \rangle(t) - \langle K \rangle(t=0) - \int_0^t \langle \text{ADVEC} \rangle dt \\ &= \int_0^t \langle \text{GSP} + \text{LSP} + \text{DSP} + \text{CP} + \text{AGSP} \\ &\quad + \text{BFLUX} \rangle dt, \end{aligned} \quad (25)$$

where the notation $\langle \cdot \rangle$ denotes a domain average and $\langle \text{PWORK} \rangle = 0$ for our choice of boundary conditions (section 4).

In section 6 we evaluate all the terms in Eq. (25) in several numerical experiments with different strain magnitudes, IW initial conditions, and vertical modes.

4. Numerical setup

The problem configuration detailed above describes a slowly evolving mean flow following the HB72 uniform PV model and a fast-evolving IW vertical mode. The IW evolution Eqs. (10a)–(10e) are solved using the pseudospectral code Dedalus (Burns et al. 2020) for two different values of imposed geostrophic strain, $\alpha = 0.04f, 0.1f$. The horizontal

wave velocities u, v are expanded using cosine expansions in the vertical to satisfy free-slip boundary conditions. The vertical wave velocity w is expanded using a sine expansion in the vertical to satisfy the rigid lid boundary conditions. The wave buoyancy b is expanded using cosine series in the vertical direction to satisfy no flux boundary conditions. All wave fields are expanded with Fourier series in the y direction because we assume a local frontal zone with all fields vanishing as $y \rightarrow \pm\infty$. Time-stepping is performed using a third-order 4-step implicit-explicit Runge-Kutta scheme with a time step of 20 s.

We add diffusivity operators of the form

$$\mathcal{D} \equiv \nu \left(\frac{\partial^2}{\partial y^2} + \frac{\partial^2}{\partial z^2} \right) - \nu_h \frac{\partial^4}{\partial y^4} \quad (26)$$

to the right-hand side of the momentum and buoyancy [Eqs. (10a), (10b), (10d)]. The inclusion of lateral hyperviscosity/hyperdiffusivity is required for numerical stability because the grid spacing in the y direction is much larger than in the z direction (Table B1 in appendix B). We refrain from using hyperviscous operators in the z direction to mimic ocean models, where vertical diffusion is elevated in the mixed layer [e.g., K -profile parameterization (KPP); Large et al. 1994]. The corresponding numerical wave KE dissipation is

$$\text{DISP} = u \mathcal{D}(u) + v \mathcal{D}(v). \quad (27)$$

In the following analysis, DISP is time integrated and domain averaged, like the other terms in Eq. (25). Details of the dimensional quantities used in the numerical simulation are given in Table B1.

5. Frontogenesis

In 2D semigeostrophic frontogenesis (HB72; Hoskins 1982), the initial frontal sharpening is dominated by the externally imposed geostrophic strain field α , leading to an exponential sharpening rate (the exponential stage). The convergent ASC that develops about the front gradually becomes stronger until it dominates the geostrophic strain, driving a superexponential sharpening rate that leads to a finite time singularity in the inviscid limit (the superexponential stage). These two growth stages are shown in Fig. 4 for two different values of α . A comparison between the α values (Figs. 4a,b) shows that as α increases, the sharpening rate also increases, and the duration of the exponential and superexponential stages are shortened. Accordingly, the frontogenesis duration reduces from 6.86 to 2.78 inertial periods as α increases from 0.04f to 0.1f. Because HB72 is an inviscid model the duration of the superexponential stage is completely determined by numerical diffusion, which prevents the finite time singularity. Therefore, to compare energy exchanges between the front and IWs during exponential and superexponential stages we compute time-averaged values of the different exchange terms [Eq. (25)] over each frontogenetic stage duration (Table 3).

Strong buoyancy gradients at frontal regions are often associated with strong divergence $\delta = \partial_y V$ and vorticity $\zeta = -\partial_y U$ signals. In semigeostrophic frontogenesis, the frontal flow is

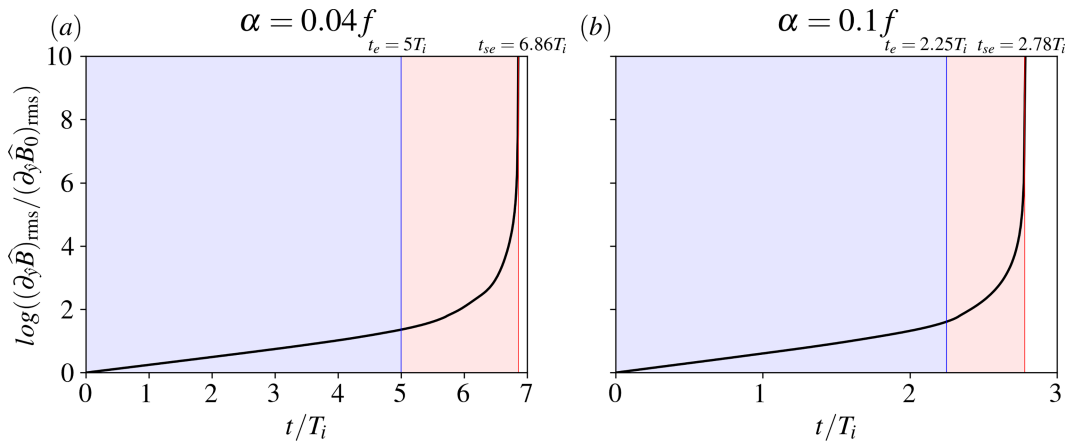


FIG. 4. The root-mean-square (rms) horizontal buoyancy gradient evolution $(\partial_y \hat{B})_{\text{rms}}$ (where $\hat{y} = y/\lambda$) computed in the frontal region for two different values of α . The frontal region is identified as the region where $(\partial_y \hat{B})^2 > 0.1(\partial_y \hat{B})_{\text{max}}^2$. The end of the exponential (denoted by t_e) and superexponential (denoted by t_{se}) frontogenetic stages are marked above the thin vertical blue and red lines, respectively. Time t is normalized by the inertial period T_i .

characterized by $\delta_{\text{rms}}/f \leq \alpha/f$ and $\text{Ro}_{\text{rms}} = \zeta_{\text{rms}}/f \leq 1$ during the exponential phase (Table 2 and Figs. 5a,b), whereas during the superexponential stage, it is characterized by $\delta_{\text{rms}}/f \gg \alpha/f$ and $\text{Ro}_{\text{rms}} \gg 1$ (Table 2 and Figs. 5c,d). In addition, $\text{Ro}_{\text{rms}} \gg \delta_{\text{rms}}/f$ at all times (the alongfront geostrophic velocity is always larger than the cross front ageostrophic velocity) with final $\delta_{\text{rms}}/f \sim \mathcal{O}(1)$. During the exponential stage, a near-perfect symmetry is observed between cyclonic/convergent and anticyclonic/divergent circulation patterns (Figs. 5a,c). One and a half inertial period later, in the superexponential stage, an asymmetry between cyclonic and anticyclonic circulation develops, with near-surface convergence and vorticity values that increase by an order of magnitude (Figs. 5b,d). During that time, the frontal width [computed in the region where $(\partial_y \hat{B})^2 > 0.1(\partial_y \hat{B})_{\text{max}}^2$, just below the surface] is decreased 50-fold. The dynamical regime during the superexponential stage, therefore, qualitatively represents surface intensified oceanic submesoscale fronts and filaments during winter months (e.g., Fig. 1).

6. Energy exchanges

The front-IW energy exchanges are explored for minimum frequency (near-inertial) and high-frequency waves (cases I and II in Fig. 3) with vertical modes 1–3 and subject to two different imposed strain values. We distinguish between energy exchanges during the exponential and superexponential

frontogenetic stages (Fig. 4), which are characteristic of oceanic mesoscale and submesoscale frontogenesis, respectively (Barkan et al. 2019).

The phase structure and KE exchanges with the mean flow are substantially different between near-inertial and high-frequency waves (Fig. 6 and Supplemental Movie 1). The NIW remains in the frontal zone because the horizontal group velocity $c_{g_y} \rightarrow 0$ [Eq. (22)], as discussed in Thomas (2012), and nearly all of its kinetic energy remains in the frontal zone during frontogenesis (Fig. 6a). This is in contrast with Rocha et al. (2018), who reported NIW energy escape from barotropic and geostrophic straining regions. Therefore, in our model, the NIWs are likely to exchange energy with the frontal circulations. On the contrary, the high-frequency wave is able to escape the frontal zone ($c_{g_y} \neq 0$), with nearly all of its energy found outside the frontal region before the superexponential stage is reached (Fig. 6d). The higher the initial IW frequency is, the faster it escapes the frontal region (e.g., the intersection between the solid and dashed magenta lines in Fig. 6d is shifted to the left by $\approx 0.2T_i$ when the initial IW frequency is increased from $1.5f$ to $3f$).

a. Case I: Minimum frequency wave (NIW)

The dominant KE exchange terms for the minimum frequency mode-1 NIW include the DSP, CP, and AGSP (Fig. 7 and Table 3). As discussed in Thomas (2012), the NIW is able to extract energy from the imposed deformation field ($\text{DSP} > 0$) when the frontal baroclinicity and vorticity modify the wave polarization relations, leading to rectilinear hodographs (i.e., $|v| > |u|$; Figs. 6c,d) and anisotropic horizontal momentum fluxes.³ The NIW loses its energy to the ASC when the wave isophases are tilted with the ageostrophic shear (solid blue line in Fig. 6d;

TABLE 2. The rms normalized vertical vorticity ($\text{Ro}_{\text{rms}} \equiv \zeta_{\text{rms}}/f$) and horizontal divergence (δ_{rms}/f) during exponential and superexponential stages of frontogenesis, computed in the frontal region (same definition as in Fig. 4) for two values of α .

Terms	$\alpha = 0.04f$		$\alpha = 0.1f$	
	$t = 5T_i$	$t = 6.8T_i$	$t = 2.25T_i$	$t = 2.7T_i$
Ro_{rms}	0.37	8.11	0.42	6.88
δ_{rms}/f	0.02	0.98	0.06	1.35

³ Specifically for a minimum frequency wave $|u|/|v| \approx (1 + \text{Ro} - \text{Ri}_g^{-1})^{1/2}$, as discussed in Whitt and Thomas (2013).

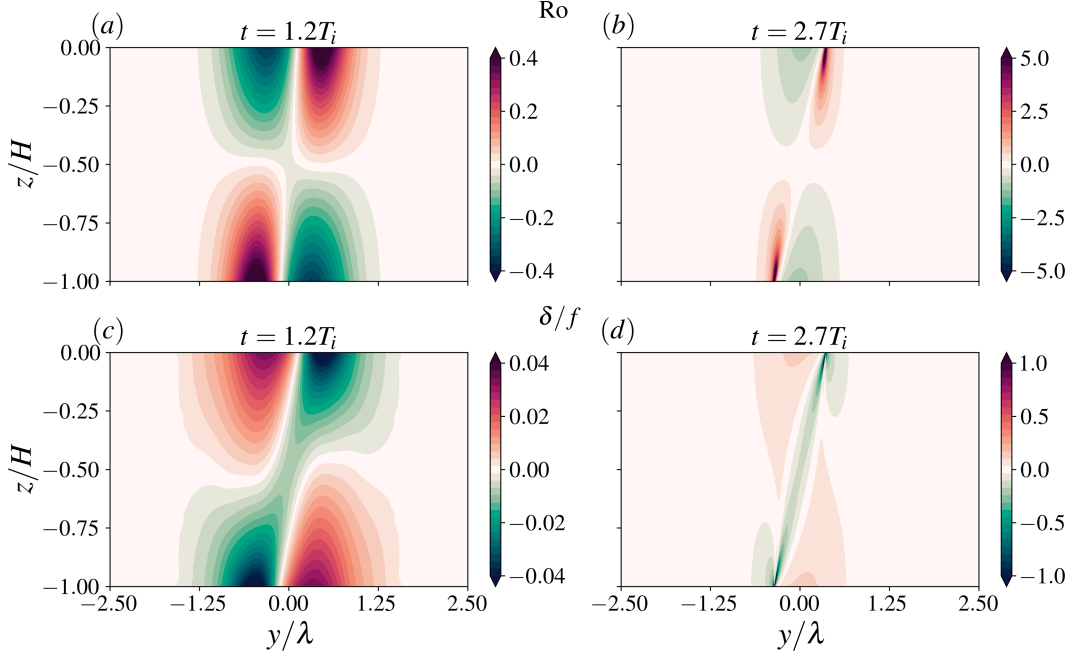


FIG. 5. Snapshots of (a),(b) the Rossby number Ro and (c),(d) the normalized horizontal divergence of the ASC δ/f , in the numerical simulation with $\alpha = 0.1f$. (left) Exponential and (right) superexponential frontogenesis stages [see Fig. 4b]. Here, T_i is the inertial period. Note the different color bar ranges between (a) and (b), and (c) and (d).

$\text{AGSP} < 0$). The AGSP is the main inviscid mechanism that drains NIW KE. This transfer of wave KE to the ASC is different from the IW reabsorption mechanism discussed in Nagai et al. (2015), which occurs due to the normal component of the Reynolds stresses (e.g., the equivalent of the CP mechanism).

The convergence production ($\text{CP} \equiv -\delta\nu^2$) is a newly identified mechanism for IW-front energy exchanges, which is associated with the convergence (or divergence) of the ASC. Convergent (divergent) regions correspond to $\text{CP} > 0$ ($\text{CP} < 0$) and wave KE gain (loss). This particular energy exchange mechanism is absent in Thomas (2012), and the QG-NIW theories (Xie and Vanneste 2015; Rocha et al. 2018; Thomas and Arun 2020), where the balanced (frontal) flow is horizontally nondivergent.

During the exponential stage, the convergence of the ASC in the frontal (cyclonic) region is rather weak and is comparable to the divergence of the ASC in the anticyclonic region (Fig. 5c). As a result, there is a cancellation when CP is domain-averaged, leading to small values compared to $\langle \text{DSP} \rangle$ (Table 3). During the superexponential stage, however, when frontal sharpening is primarily driven by the convergence of the ASC [$|\delta/f| \sim \mathcal{O}(1)$; Fig. 5d], CP gradually begins to dominate the NIW KE gain (red and blue lines in Fig. 7, red shading). Quantitatively, when time-averaged over the superexponential stage only, $\langle \text{CP} \rangle > \langle \text{DSP} \rangle$ for all simulated strain values (Table 3). This CP dominance is particularly evident when the DSP and CP terms are averaged separately inside and outside the frontal zone (denoted by F and OF , respectively; Fig. 8).

Inside the frontal zone the time-integrated $\langle \text{CP} \rangle_F$ increases rapidly, in concert with the increased convergence of the ASC

(Figs. 5c,d), and dominates $\langle \text{DSP} \rangle_F$ (solid red and blue lines in Fig. 8, red shading). In fact, because the imposed strain is constant everywhere, the DSP magnitude is approximately the same inside and outside of the frontal region (solid and dashed blue lines in Fig. 8). Furthermore, the cancellation between the positive $\langle \text{CP} \rangle_F$ and negative $\langle \text{CP} \rangle_{OF}$ values are clearly evident during the exponential stage (solid and dashed red lines in Fig. 8, blue shading). The AGSP, which like CP is determined by the magnitude of the ASC, is considerably more negative when averaged inside the frontal zone (solid and dashed green lines in Fig. 8). Interestingly during the superexponential stage of frontogenesis the loss of wave KE to the ASC via the AGSP is partially compensated for by KE gain from the ASC via the CP (Table 3). We explain this result below.

The contribution of $\langle \text{BFLUX} \rangle$ is small in both stages of the frontogenesis. This is in contrast with the theory of Xie and Vanneste (2015), where $\text{BFLUX} < 0$ converts Eulerian-mean NIW KE to wave PE (Rocha et al. 2018). The reason for such a small value of BFLUX is explained in section 6a(1). Finally, the remaining energy exchange terms in Eq. (23) remove a small amount of NIW KE during both frontogenetic stages (Table 3).

1) SPATIAL STRUCTURE OF THE ENERGY EXCHANGE TERMS

To gain further insight into the IW-front energy exchanges, we examine the spatial structure of the various KE exchange terms in Eq. (23) during the exponential and superexponential

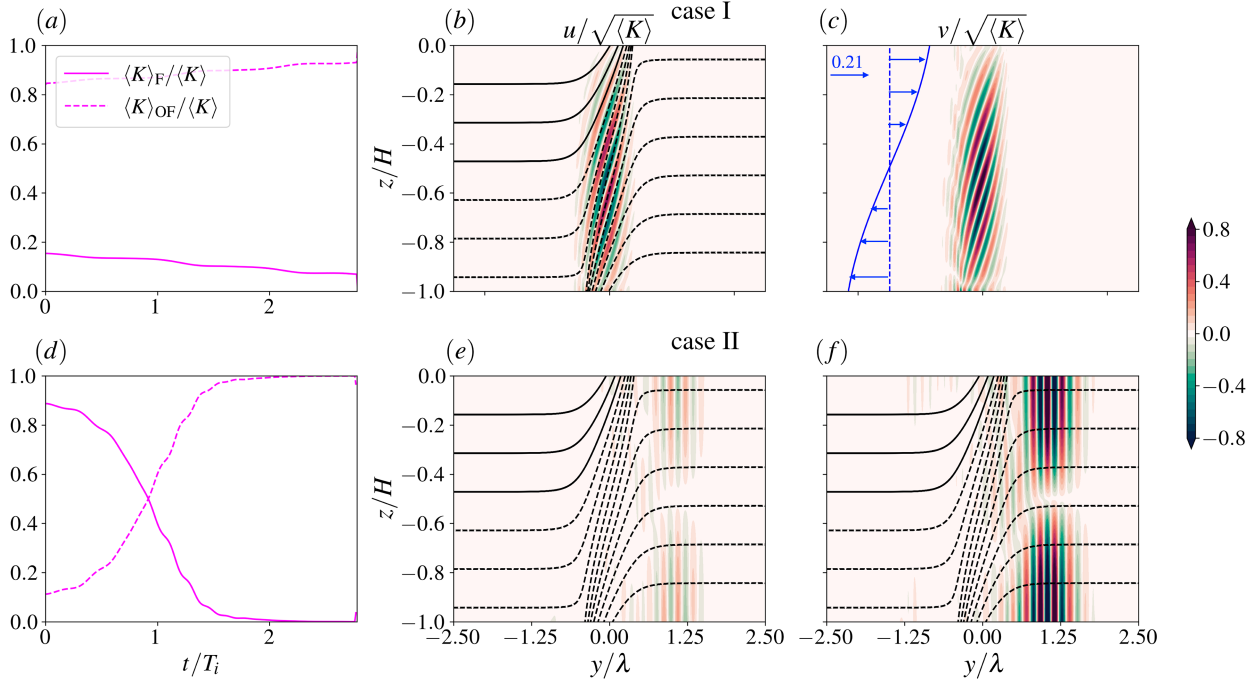


FIG. 6. The wave kinetic energy fractions inside the frontal region ($\langle K_F \rangle / \langle K \rangle$) and outside of it ($\langle K_{OF} \rangle / \langle K \rangle$) are shown for (a) minimum frequency (case I) and (d) high-frequency (case II) waves. The frontal region is identified as the region where $(\partial_y \hat{B})^2 > 0.1(\partial_y \hat{B})_{\max}^2$, where $\hat{y} = y/\lambda$. Snapshots of mode-1 IW velocity components (b),(e) u and (c),(f) v [normalized by corresponding $\sqrt{\langle K(t) \rangle}$] are plotted at $t = 2T_i$ based on a simulation with $\alpha = 0.1f$. Panels (b) and (c) correspond to case I, and (e) and (f) correspond to case II. The black contour lines in (b), (e), and (f) display \hat{B} [Eq. (9c)] with a 0.26 contour interval (solid and dotted lines show positive and negative values, respectively). Blue arrows in (c) indicate the profile of the horizontal component of the ASC, \hat{V} [Eq. (38b)], at $y = 0$, illustrating that the ageostrophic vertical shear is tilted with the IW phase lines.

frontogenetic stages (Figs. 9 and 10, respectively) for a mode-1 NIW (case I; section 6a) with $\alpha = 0.1f$.

The time-integrated DSP is predominantly positive during both frontogenetic stages because of the rectilinear wave

hodographs (Figs. 6b,c), and is concentrated in the frontal (cyclonic) region (Figs. 5a,b). As the front sharpens the positive DSP signal is confined to a smaller area with larger value during the superexponential stages (Figs. 9c and 10c), in

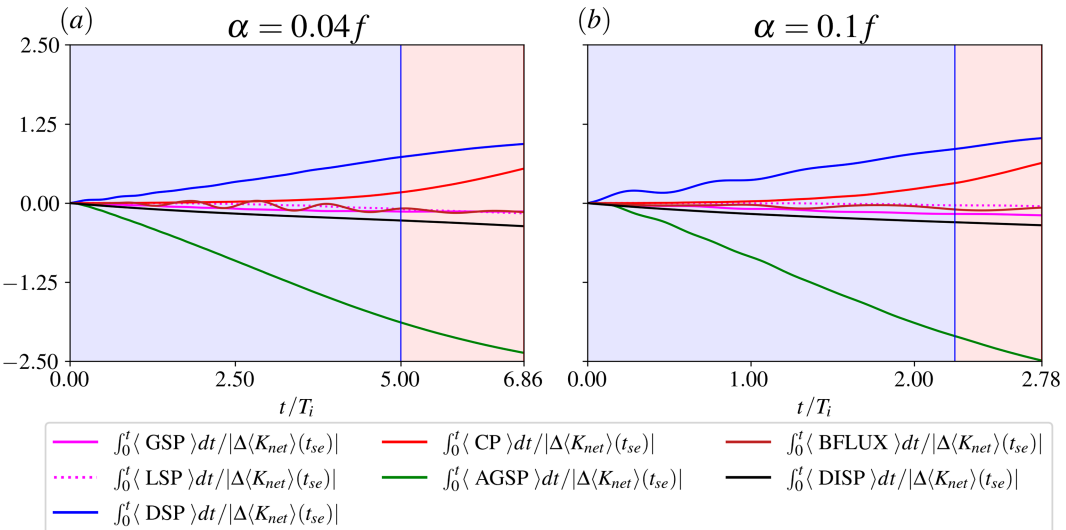


FIG. 7. The various terms in the IW KE evolution Eq. (23) for numerical simulations with different α values and a mode-1 IW, which is initially near inertial (case I). The end of the exponential and superexponential frontogenetic stages are denoted by the thin vertical blue and red lines, respectively. Time is normalized by the inertial period T_i .

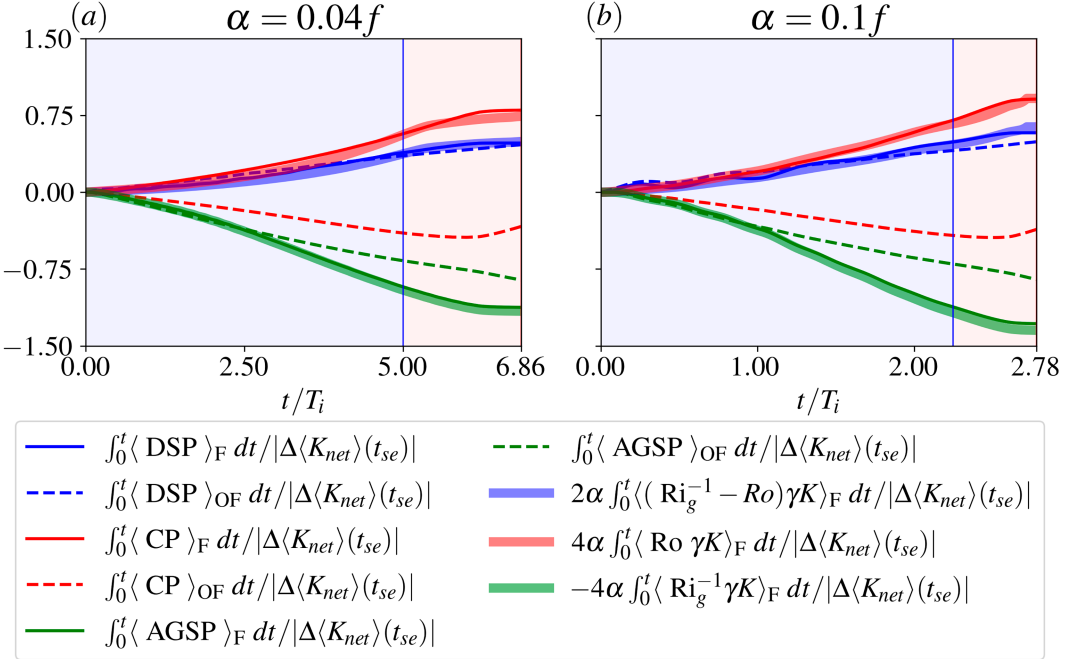


FIG. 8. The DSP, CP, and AGSP terms (thin lines) in the IW KE evolution Eq. (23) for a mode-1 minimum frequency IW (case I) with two initial strain magnitudes [(a) $0.04f$, (b) $0.1f$]. The exchange terms are averaged separately over frontal regions (subscript F ; solid lines) and outside the frontal region (subscript OF ; dashed lines). The thick lines show the theoretical predictions for DSP, CP, and AGSP [Eqs. (38a)–(38c)], averaged over the frontal region. The blue (red) shaded region shows the exponential (superexponential) frontogenetic stage. Time is normalized by the inertial period T_i . Frontal regions are defined as in Fig. 4.

agreement with Table 3. The time-integrated AGSP is negative during both stages because the wave phase lines are tilted with the ageostrophic shear (Figs. 6a,b), and is even more tightly confined to the frontal region. Similarly to the DSP, it occupies a smaller region as the front sharpens with larger magnitudes in the superexponential frontogenetic stage (Figs. 9e and 10e).

The cancellation between positive CP in the frontal region and negative CP outside the frontal region during the exponential stage (red lines in Fig. 8b) is clearly visible in the spatial plot (Fig. 9d). As the convergent ASC strengthens during the superexponential stage (Fig. 6d), CP becomes strongly positive in the frontal region and dominates the negative signal outside the front (Fig. 10d), leading to a domain-averaged positive contribution (Fig. 7b and Table 3).

The time-integrated LSP is everywhere an order of magnitude smaller than the remaining terms (Figs. 9b and 10b), as expected from Table 3. The time-integrated BFLUX term however (Figs. 9f and 10f) exhibits similar magnitudes to the other terms, albeit with both positive and negative lobs that cancel out when averaged over the entire domain (Table 3). This is because the wave isophases are not exactly parallel to isopycnals but, in fact, have a shallower slope (Figs. 3a,b). Because the total buoyancy $B + b$ is conserved (as shown below), the wave must acquire a positive (negative) buoyancy anomaly b in the region of lower (higher) B . In turn, regions of positive (negative) b are associated with an increase

(decrease) in wave PE and consequently, $\text{BFLUX} < 0$ ($\text{BFLUX} > 0$). Interestingly, the integrated GSP term has similar spatial structures to the integrated BFLUX term during both frontogenetic stages, albeit with opposite signs (Figs. 9a,f and 10a,f).

To understand this feature in our solutions, we examine the evolution of the total absolute momentum $M = u + U - fy$ together with the total buoyancy $B + b$, in the inviscid nondifusive limit. For time scales sufficiently smaller than α^{-1} , it is safe to assume that both the total absolute momentum and total buoyancy are nearly conserved. Following Whitt and Thomas (2013), the x component of the wave velocity u can be written as

$$u(t + \delta T) - u(t) = -\nabla M_g \cdot \delta \mathbf{r} = -\left(\frac{\partial M_g}{\partial y} \delta Y + \frac{\partial M_g}{\partial z} \delta Z\right), \quad (28)$$

where $M_g = U - fy$ is the absolute momentum of the geostrophic flow, $\delta \mathbf{r} = \hat{y} \delta Y + \hat{z} \delta Z$ denotes the position vector such that $\delta Y = \int_t^{t+\delta T} v dt$ and $\delta Z = \int_t^{t+\delta T} w dt$, and $\delta T < \alpha^{-1}$ is the time duration. Similarly, it follows that the wave buoyancy b can be expressed as

$$b(t + \delta T) - b(t) = -\nabla B \cdot \delta \mathbf{r} = -\left(\frac{\partial B}{\partial y} \delta Y + \frac{\partial B}{\partial z} \delta Z\right). \quad (29)$$

Using Eq. (28), the GSP can be written as

TABLE 3. The various energy exchange terms in the IW KE evolution Eq. (25), time-averaged over the exponential and superexponential frontogenetic stages (blue and red shading in Fig. 4), for a mode-1, minimum frequency IW (case I) subject to different α values. The time integration is from $t_0 = 0$ to $t = t_e$ for the exponential stage, and from $t_0 = t_e$ to $t = t_{se}$ for the superexponential stage, where t_e and t_{se} denote the end of the exponential and the superexponential stage, respectively. The energy exchange terms are normalized by the magnitude of the net KE exchange over the integration time, $|\Delta\langle K_{net}\rangle(t_{se})|$ and time is normalized by the inertial period T_i . Angle brackets denote a domain average. Similar qualitative results are obtained for higher-mode NIWs (see supplemental material). The bold values highlight quantities that are significant compared to the others.

Terms	Exponential		Superexponential	
	$\alpha = 0.04f$	$\alpha = 0.1f$	$\alpha = 0.04f$	$\alpha = 0.1f$
$\frac{T_i}{t - t_0} \int_{t_0}^t \langle \text{GSP} \rangle dt / \Delta\langle K_{net}\rangle(t_{se}) $	-0.03	-0.05	0.02	0.05
$\frac{T_i}{t - t_0} \int_{t_0}^t \langle \text{LSP} \rangle dt / \Delta\langle K_{net}\rangle(t_{se}) $	-0.01	-0.01	-0.02	-0.04
$\frac{T_i}{t - t_0} \int_{t_0}^t \langle \text{DSP} \rangle dt / \Delta\langle K_{net}\rangle(t_{se}) $	0.15	0.37	0.11	0.34
$\frac{T_i}{t - t_0} \int_{t_0}^t \langle \text{CP} \rangle dt / \Delta\langle K_{net}\rangle(t_{se}) $	0.06	0.14	0.21	0.58
$\frac{T_i}{t - t_0} \int_{t_0}^t \langle \text{AGSP} \rangle dt / \Delta\langle K_{net}\rangle(t_{se}) $	-0.38	-0.93	-0.26	-0.71
$\frac{T_i}{t - t_0} \int_{t_0}^t \langle \text{BFLUX} \rangle dt / \Delta\langle K_{net}\rangle(t_{se}) $	-0.02	-0.04	-0.06	-0.03
$\frac{T_i}{t - t_0} \int_{t_0}^t \langle \text{DISP} \rangle dt / \Delta\langle K_{net}\rangle(t_{se}) $	-0.02	-0.05	-0.05	-0.04

$$-uw \frac{\partial U}{\partial z} \Big|_{t+\delta T} = -[u(t) - \nabla M_g \cdot \delta \mathbf{r}] w \frac{\partial M_g}{\partial z}, \quad (30)$$

and using Eq. (29), the BFLUX can be expressed as

$$wb|_{t+\delta T} = w[b(t) - \nabla B \cdot \delta \mathbf{r}]. \quad (31)$$

To compute the approximate GSP and BFLUX above we begin with the initial conditions described in section 2b and time step Eqs. (28) and (29) to obtain u and b at all times. Equations (30) and (31) are then calculated every 10 min using the numerical values of v , w , M_g , and B . The approximate GSP and BFLUX fields, time integrated separately over the exponential and superexponential stages, are shown as contour lines in Figs. 9a, 9f, 10a, and 10f, respectively. The close resemblance between the approximate and true fields suggests that the spatial structures of the GSP and BFLUX in our solutions are a result of the conservation of total absolute momentum and total buoyancy, respectively.

2) THE PARTIAL CANCELLATION BETWEEN CP AND AGSP DURING THE SUPEREXPONENTIAL STAGE

An interesting feature in our solution is that during the superexponential stage of frontogenesis, the loss of wave KE due to the AGSP mechanism is partially compensated by the KE gained from ASC via CP (solid red and green lines in the red-shaded region of Figs. 8 and 10d,e). This can be better understood by projecting the wave momentum flux in the direction of the principal strain axes of the ASC. In general, the

sum of CP and AGSP in the principal strain coordinates can be expressed as

$$\text{CP} + \text{AGSP} = \frac{1}{2}(v'^2 + w'^2) \left(\frac{\partial V}{\partial y} + \frac{\partial W}{\partial z} \right) - (v'^2 - w'^2) \frac{S'_n}{2}, \quad (32)$$

where v' , w' are velocity components in the transformed coordinates, given by

$$v' = v \cos \theta_p + w \sin \theta_p, \quad (33a)$$

$$w' = -v \sin \theta_p + w \cos \theta_p, \quad (33b)$$

and S'_n is

$$S'^2_n = \left(\frac{\partial V}{\partial y} - \frac{\partial W}{\partial z} \right)^2 + \left(\frac{\partial V}{\partial z} + \frac{\partial W}{\partial y} \right)^2. \quad (34)$$

The angle between the simulated coordinates and the principal strain coordinates $\theta_p(y, z)$ is given by

$$\tan 2\theta_p = \frac{\partial V/\partial z + \partial W/\partial y}{\partial V/\partial y - \partial W/\partial z} \approx \frac{\partial V/\partial z}{2\partial V/\partial y}, \quad (35)$$

where the last step assumes $(\partial W/\partial y) \ll (\partial V/\partial z)$, consistent with our numerical solutions.

Because our model is x invariant, the first term on right-hand side of Eq. (32) is zero, and so

$$\text{CP} + \text{AGSP} = (w'^2 - v'^2) \frac{S'_n}{2}. \quad (36)$$

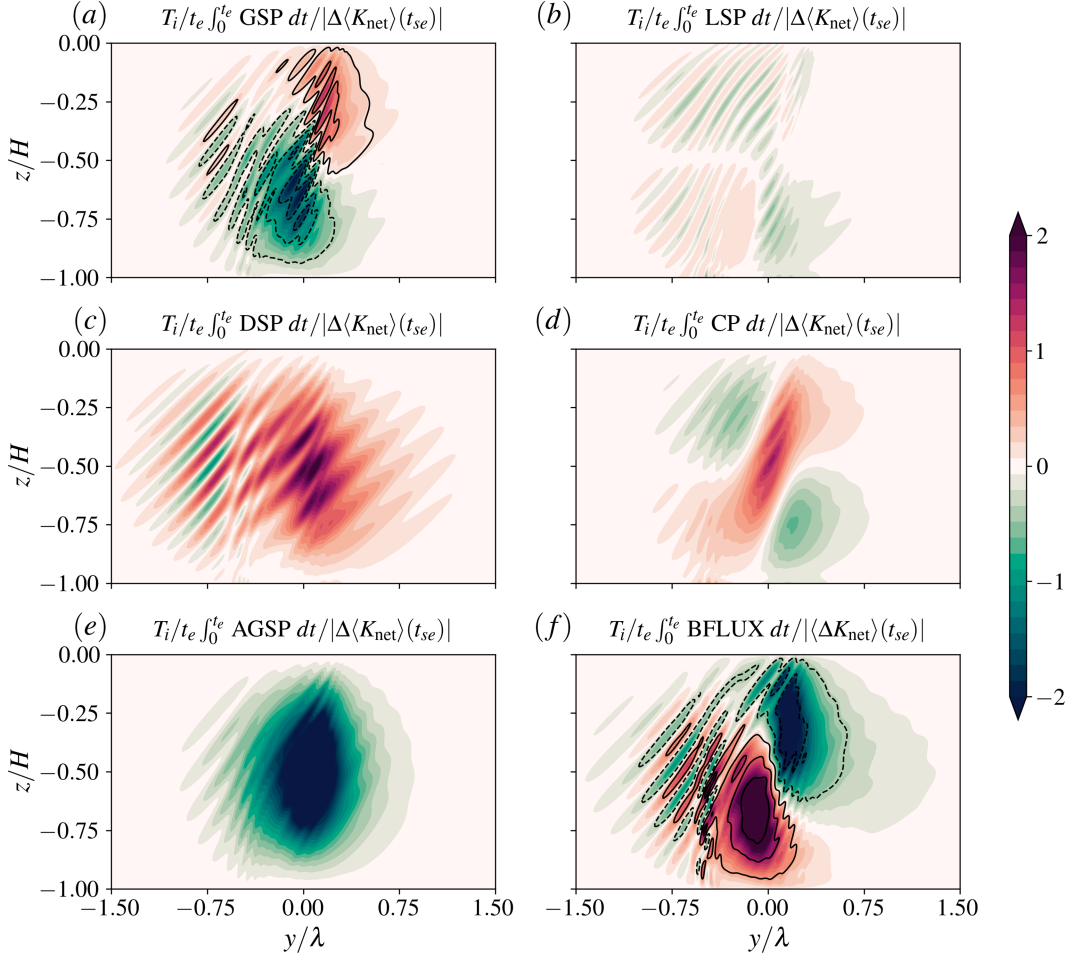


FIG. 9. (a)–(f) The various terms in the IW KE evolution Eq. (23) integrated and time-averaged over the exponential frontogenetic stage (blue shading in Fig. 4; t_e and t_{se} denote the end of exponential and superexponential stages, respectively), for a mode-1, minimum frequency IW (case I), subject to $\alpha = 0.1f$. The approximate GSP and BFLUX values in Eqs. (30) and (31) are shown with contour lines in (a) and (f), respectively, where solid (dashed) lines denote positive (negative) values with a 2.56 contour interval for GSP and a 2.14 contour interval for BFLUX. All fields are normalized by the domain-averaged net KE exchange $\Delta\langle K_{\text{net}} \rangle(t_{se})$ [Eq. (25)], and time is normalized by the inertial period T_i .

When $w'^2 = v'^2$, the wave-induced momentum flux in the principal strain coordinates vanishes, and CP and AGSP have equal and opposite signs. In this case $\tan 2\theta_p \approx -v/(2w)$ and, together with Eq. (35), we obtain $w/v = (\partial W/\partial z)/(\partial V/\partial z)$. This implies that the net KE exchanges between NIWs and the ASC are zero only when the phase lines of the NIWs are aligned with the streamlines of the ASC. This particular condition is nearly met during the superexponential stage, as the ASC streamlines align more closely with the isopycnals, and hence with the isophases of the NIWs (Figs. 11a,b).

b. Case II: High-frequency wave

Thomas (2012) demonstrated that higher-frequency IWs gradually approach the minimum frequency as the front sharpens. In this process, however, the wave phase lines become nearly vertical (Figs. 6e,f), and the intrinsic horizontal

group velocity $c_{g,y} \rightarrow \pm N/m_n$ [Eq. (22)], allowing the wave to escape the frontal region. Due to our configuration setup, the IW is unable to propagate out of the imposed-strain influence, as in Thomas (2019), and is instead halted where $-c_{g,y} = (V - \alpha y)$ (see also Supplemental Movie 2). Consequently, the KE exchange terms with the front are substantially different than for NIW (case I), where energy exchanges are confined to the frontal region. The IW still gains energy through the ⟨DSP⟩, as the hodographs remain rectilinear (cf. Figs. 6e,f), but this happens outside of the frontal region (blue dot-dashed line in Fig. 12b). This is because the imposed strain, α , acts to reduce u^2 and induce stronger v^2 , which leads to a positive correlation between α and $(v^2 - u^2)$ (Jing et al. 2017). The ⟨BFLUX⟩ is now strong and negative (brown lines in Fig. 12), implying that the wave KE is converted to wave PE. This is consistent with the finding of Rocha et al. (2018), where it is shown that the

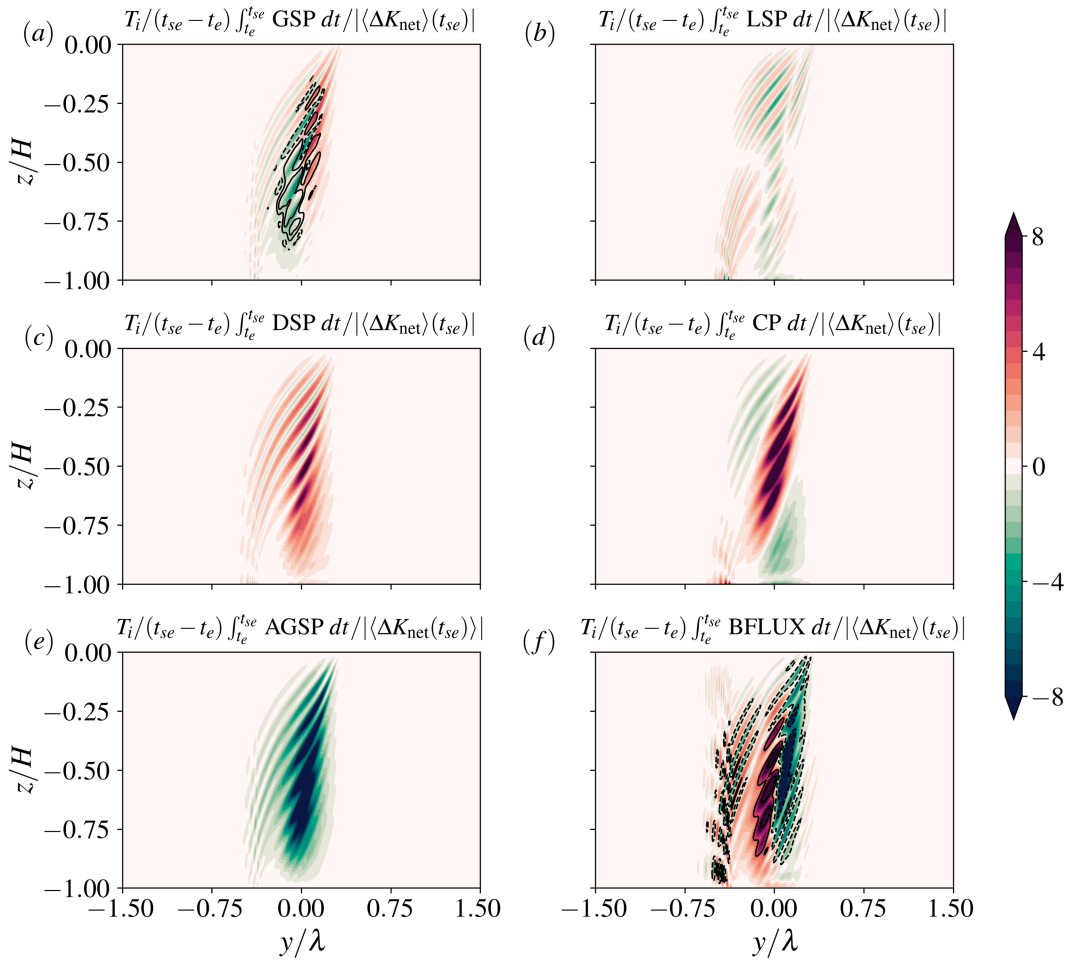


FIG. 10. As in Fig. 9, but time-integrated over the superexponential frontogenetic stage (red shading in Fig. 4). The contour intervals in (a) and (f) are 2.68 and 5.34 for the approximate GSP in Eq. (30) and BFLUX in Eq. (31), respectively.

decrease in the horizontal length scale of the wave leads to an increase in wave PE and a subsequent reduction in the Lagrangian-mean balanced kinetic energy. Mechanistically, if the IW phase lines are to remain vertical and steeper than the isopycnals (Figs. 6e,f and supplemental material), then it must, on average, accumulate PE.

7. Summary and discussion

The present study is focused on the energy exchanges between a two-dimensional front undergoing strain-induced semigeostrophic frontogenesis described by HB72 and hydrostatic, linear IW vertical modes. The main novelties of the study are

- 1) the IWs are no longer unbounded in the vertical (e.g., Thomas 2012) and have a modal structure that is more representative of oceanic IWs, and
- 2) the energy exchanges are quantified in a flow regime of $\text{Ro} \sim \mathcal{O}(1)$, and strong horizontal convergent motion, $|\delta|/f \sim \mathcal{O}(1)$, representative of oceanic submesoscale fronts and filaments.

The model is solved numerically for two different strain values and IW vertical modes 1–3 that are initially oriented parallel to isopycnals (case I, minimum frequency NIW) or tilted against isopycnals (case II, high-frequency IWs, $\omega = 1.5f$). For all of our solutions, we compute the various terms in the wave KE Eq. (25), distinguishing between the exponential and superexponential frontogenetic stages.

In agreement with previous work (Thomas 2019), high-frequency waves can escape the frontal zone and, therefore, exchange little energy with the ageostrophic frontal circulation. Nevertheless, because the imposed strain is also acting outside of the frontal zone, the high-frequency wave can still efficiently extract KE from the balanced deformation flow through the DSP mechanism.

NIW also extract KE from the balanced deformation flow via the deformation shear production (DSP) because the imposed strain and baroclinicity modify the wave hodographs to be rectilinear (Thomas 2012). In contrast with high-frequency IWs, however, NIW modes remain in the frontal zone and can exchange KE with the ageostrophic frontal flow because

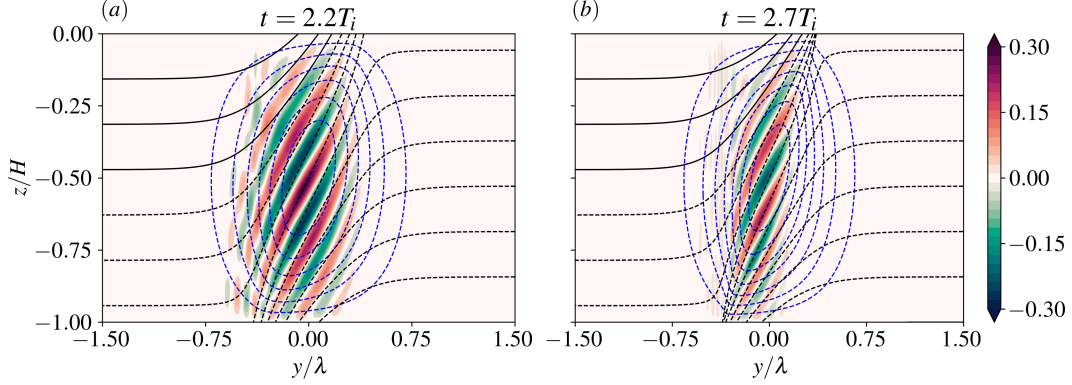


FIG. 11. Snapshots of the NIWs streamfunction χ [normalized by $\sqrt{K(t)}H$; color shading] with superimposed non-dimensional buoyancy \hat{B} [Eq. (38c); black lines] with a 0.26 contour interval, and ASC nondimensional streamfunction $\hat{\Psi}$ [Eq. (38d); blue lines] with a 0.08 contour interval during (a) exponential ($t = 2.2T_i$, Fig. 4b) and (b) superexponential ($t = 2.7T_i$) stages of the frontogenesis. The solid and dotted lines show positive and negative values, respectively. Based on a numerical simulation with $\alpha = 0.1f$.

their phase lines align with isopycnals and their group velocity $c_{g_y} \rightarrow 0$. Indeed, during the exponential stage, most of the KE extracted due to DSP is transferred to the frontal ageostrophic secondary circulation (ASC) via the ageostrophic shear production (AGSP), because the wave phase lines are tilted with the ageostrophic vertical shear. The inclusion of $\text{Ro} \sim \mathcal{O}(1)$ and ageostrophic convergent motions in our model allows us to identify a new mechanism, the convergence production (CP), through which NIWs can efficiently exchange KE with the frontal ASC. The sign of this energy transfer is shown to depend on the sign of the horizontal divergence of the mean flow. We demonstrate that CP dominates the energy exchanges in the frontal region during the superexponential stage when the convergent ASC inside the frontal zone increases [$|\delta|/f \sim \mathcal{O}(1)$] and leads to a domain

averaged positive value despite a weak negative contribution from divergent flow outside of it. Furthermore, we demonstrate that during the superexponential stage, the KE loss due to the AGSP is largely compensated for by a KE gain due to the CP. This is because as the front sharpens during the superexponential stage, the ASC streamlines align more closely with isopycnals, and hence the phase lines of the NIWs. Thus, there is a natural tendency for the wave momentum flux to align with ASC streamlines, which is less effective at fluxing the momentum of the ASC and at inducing KE transfers between the NIW and the ASC.

a. Oceanic implications

The importance of horizontal divergence to IW energetics has been previously discussed in Weller (1982), albeit in a

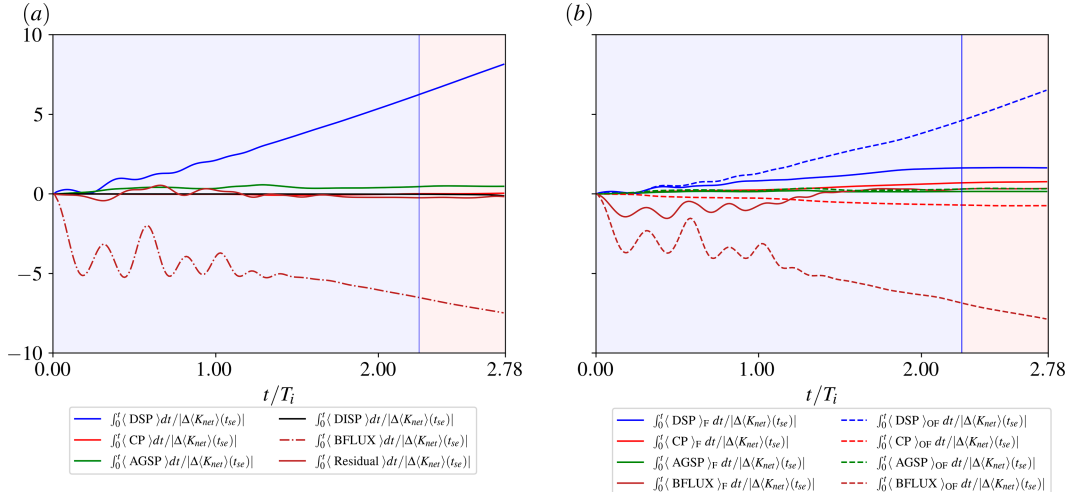


FIG. 12. (a) The various terms in the IW KE evolution Eq. (23) for numerical simulation with $\alpha = 0.1f$ for a mode-1 high-frequency IW ($\omega = 1.5f$; case II). Note that the residual = GSP + LSP. (b) The different energy exchange terms averaged over the frontal region are defined as the region where $(\partial_y \hat{B})^2 > 0.1(\partial_y \hat{B})_{\max}^2$, $\hat{y} = y/\lambda$ (subscript F; solid lines) and outside the frontal region (subscript OF; dashed lines). The blue (red) shaded region shows the exponential (superexponential) frontogenetic stage. Time is normalized by the inertial period T_i .

regime of weak divergent QG flow. Barkan et al. (2021) demonstrated, using realistically forced high-resolution numerical simulations in the North Atlantic Ocean, that the most substantial energy transfers from balanced flow to IWs occur at surface intensified fronts and filaments that are characterized by $\text{Ro} \sim \mathcal{O}(1)$ and strong ageostrophic convergent motions. The results presented here suggest that CP may explain these observed energy transfers.

To further interpret our results in the context of realistic ocean models and field measurements we provide analytical estimates for the most dominant energy exchange terms between NIWs and the mean flow in our solutions; the DSP, CP, and AGSP [Eq. (23)]. Using the HB72 scaling for the along-front and cross front velocity components [Eq. (9)], the horizontal divergence and ageostrophic vertical shear take the form

$$\delta = -2\alpha\text{Ro}, \quad (37a)$$

$$\frac{\partial V}{\partial z} = 2\alpha \frac{S^2}{f^2}, \quad (37b)$$

where we emphasize that $\delta = \partial_y V$, $\text{Ro} = -\partial_y U/f$, and $S^2 = -\partial_y B$ are based on the local flow gradients. The NIW wave velocity magnitudes are determined by the polarization relations for minimum frequency IWs [Eq. (21b)], and the corresponding energy exchange terms can be written as

$$\text{DSP} = 2\alpha(\text{Ri}_g^{-1} - \text{Ro})\gamma K, \quad (38a)$$

$$\text{CP} = 4\alpha\text{Ro}\gamma K, \quad (38b)$$

$$\text{AGSP} = -4\alpha\text{Ri}_g^{-1}\gamma K, \quad (38c)$$

where $\gamma = (1/2v^2)/K = 1/(2 + \text{Ro} - \text{Ri}_g^{-1})$ denotes the fraction of wave KE associated with the cross-front wave velocity v . For NIWs in a cyclonic and convergent frontal zone $\text{Ro} > 0$, $\text{Ri}_g^{-1} > 0$ and $(\text{Ri}_g^{-1} - \text{Ro}) > 0$, and so DSP, CP > 0 and AGSP < 0. Indeed, the above analytical predictions match well the computed energy exchanges in the frontal region (thick solid lines in Fig. 8).

Evidently, Eqs. (38a)–(38c) only hold exactly in our idealized frontogenesis model and should be viewed as scaling estimates for more realistic model solutions or in situ measurements. Importantly, they illustrate the dependency of the energy exchanges on the IW kinetic energy content and the mean-flow parameters Ro and Ri_g . For example, the condition for the frequency of a NIW in a cyclonic frontal region to be real [Eq. (21a)] is $(\text{Ri}_g^{-1} - \text{Ro}) < 1$. Using this condition in Eq. (38a) results in the upper bound $\text{DSP} < 2\alpha\gamma K$, which demonstrates that the energy extraction by the NIW due to DSP depends on the “mesoscale” strain rate α and the eccentricity of the wave hodographs (i.e., γ). On the contrary, CP and AGSP depend directly on Ro and Ri_g^{-1} , which are expected to grow as the front sharpens. Like DSP, AGSP also depends on the wave orientation because the efficiency of this energy exchange mechanism crucially depends on the cross-front wave velocity aligning with the ageostrophic frontal shear. In a three-dimensional frontal zone, Srinivasan et al.

(2022) demonstrated that the CP mechanism should take the general form

$$\text{CP} = -\delta K, \quad (39)$$

where the current divergence is $\delta = \partial_x U + \partial_y V$, and K is the KE of the IWs. This coordinate-invariant form of CP illustrates that the theoretical prediction in Eq. (38b) should generalize to

$$\text{CP} \sim \alpha\text{Ro}K, \quad (40)$$

and that the magnitude and direction of the exchange should only depend on the magnitude and sign of Ro (and the wave kinetic energy) and not on the wave orientation relative to the front.

It was shown in Barkan et al. (2019) that the dynamical dominance of the convergent ASC in submesoscale fronts and filaments observed and modeled in the northern Gulf of Mexico is independent of the physical mechanism that initiated frontogenesis (e.g., mesoscale strain or turbulent thermal wind; Gula et al. 2014). This means that, in contrast with the DSP, CP can lead to energy extraction from oceanic fronts even in the absence of mesoscale straining motions. Furthermore, it was demonstrated that the frontal convergence rate $-\delta/f \sim \text{Ro}$ (see also D’Asaro et al. 2018), which is substantially stronger than predicted by the HB72 model used here. This means that, in effect, CP can be $\mathcal{O}(f/\alpha)$ larger than in Eq. (40).

For the high-frequency IW, we show in appendix C that the theoretical estimates for the dominant energy exchange terms take the form

$$\text{DSP} = \alpha(v^2 - u^2), \quad (41a)$$

$$\text{BFLUX} = -\alpha v^2 \quad (41b)$$

In this case, the eccentricity of the wave hodographs is solely a result of the imposed strain because the high-frequency wave escapes the frontal zone and does not feel the baroclinicity of the flow. As time progresses the wave hodographs become more rectilinear ($|v| \gg |u|$), $\text{DSP} \approx \alpha v^2$ and $\text{BFLUX} \approx -\text{DSP}$, as is shown in Fig. 12b (dashed blue and brown lines).

b. Final remarks

The idealized 2D model used here ignores a variety of oceanic processes that can interfere and/or coexist with the energy exchange mechanisms we discuss. The rapid increase in the horizontal convergence of the ASC during the superexponential stage is arrested in reality by frontal instabilities like symmetric instability (Thomas and Lee 2005; Yu et al. 2019), that are excited at $\mathcal{O}(100)\text{m}$ scales (Dong et al. 2021), or by boundary layer turbulence (Munk et al. 2000). Furthermore, IWs can radiate downward into the ocean interior (Thomas 2019) or transfer their energy to higher-frequency waves (higher modes) via nonlinear wave-wave interactions (McComas and Bretherton 1977). A more complete investigation of the KE

exchange mechanisms in realistic ocean simulations is left for a future study.

Acknowledgments. SK and RB were supported by Israeli Science Foundation Grant 1736/18. RB was further supported by NSF Grant OCE-1851397. The authors report no conflicts of interest.

Data availability statement. The numerical code used to generate the data is available at <https://github.com/subhk/NIW-2Dfront>.

APPENDIX A

Derivation of the HB72 Model

The governing equations of the mean-flow evolution are given by

$$\frac{DU}{Dt} - fV + \alpha U = 0, \quad (\text{A1a})$$

$$\frac{DV}{Dt} + fU - \alpha V = -\frac{\partial P}{\partial y}, \quad (\text{A1b})$$

$$0 = -\frac{\partial P}{\partial z} + B, \quad (\text{A1c})$$

$$\frac{DB}{Dt} = 0, \quad (\text{A1d})$$

$$\frac{\partial V}{\partial y} + \frac{\partial W}{\partial z} = 0, \quad (\text{A1e})$$

where the material derivative is defined as

$$\frac{D}{Dt} \equiv \frac{\partial}{\partial t} + (V - \alpha y) \frac{\partial}{\partial y} + W \frac{\partial}{\partial z}. \quad (\text{A2})$$

Using generalized momentum coordinates defined in Eqs. (5), Eqs. (A1a) and (A1b) can be combined into

$$\frac{\partial^2 U}{\partial T^2} + (f^2 - \alpha^2)U = f^2 U_g, \quad (\text{A3})$$

where the vertical advection terms are discarded because their contributions appear at $\mathcal{O}[(\alpha/f)^2]$ which is negligible since in the HB72 model $\alpha \ll 1$, except when the finite-time singularity is reached (Shakespeare and Taylor 2013). The materially conserved PV [Eq. (4)] in the generalized momentum coordinate system [Eqs. (5a)–(5c)] takes the form

$$\frac{Dq}{DT} = 0, \quad (\text{A4a})$$

$$q(Y, Z, T) = f \frac{\partial B}{\partial Z} \left(1 + \frac{1}{f} e^{\alpha T} \frac{\partial U}{\partial Y} \right)^{-1}, \quad (\text{A4b})$$

where the generalized material derivative is defined as

$$\frac{D}{DT} = \frac{\partial}{\partial T} + W \frac{\partial}{\partial Z}. \quad (\text{A5})$$

We pick an initial uniform PV distribution $q(Y, Z, T = 0) \equiv q_0 = fN^2$, and Eq. (A4b) become

$$f \frac{\partial B}{\partial Z} - q_0 \left(1 + \frac{1}{f} e^{\alpha T} \frac{\partial U}{\partial Y} \right) = 0. \quad (\text{A6})$$

The buoyancy equation at the top and bottom boundaries is given by

$$\frac{\partial B}{\partial T} = \frac{\partial \Delta B}{\partial T} = 0, \quad (\text{A7})$$

and the assumption of a localized front gives $\Delta B(Y \rightarrow \pm\infty, Z, T) = 0$. Using this condition, Eq. (A7) yields $\Delta B(Y, Z = 0, T) = \Delta B(Y, Z = -H, T) = 0$. Substituting Eq. (6) into the PV conservation Eq. (A6), and applying the boundary condition $\Delta B = 0$ at $Z = -H$ yields

$$\Delta B(Y, Z, T) = \frac{N^2}{f} e^{\alpha T} \int_{-H}^Z \frac{\partial U}{\partial Y} dZ'. \quad (\text{A8})$$

Thus the total buoyancy field B can be expressed as

$$B(Y, Z, T) = N^2 Z + B_0(Y) + \frac{N^2}{f} e^{\alpha T} \int_{-H}^Z \frac{\partial U}{\partial Y} dZ'. \quad (\text{A9})$$

Combining Eqs. (A1d) and (A9) we obtain an expression for the vertical velocity W

$$W = -\frac{J}{f} e^{-\alpha T} \int_{-H}^Z \frac{\partial}{\partial T} \left(e^{\alpha T} \frac{\partial U}{\partial Y} \right) dZ', \quad (\text{A10a})$$

$$J = e^{\alpha T} \left(1 + \frac{1}{f} e^{\alpha T} \frac{\partial U}{\partial Y} \right)^{-1}. \quad (\text{A10b})$$

It is convenient to introduce an ageostrophic secondary circulation (ASC) streamfunction $\Psi(Y, Z, T)$ as

$$\Psi = - \int_{-\infty}^Y W J^{-1} dY = \frac{1}{f} e^{-\alpha T} \frac{\partial}{\partial T} \left(e^{\alpha T} \int_{-H}^Z dZ' U \right), \quad (\text{A11})$$

where for evaluating the Y integral of the above equation we assume that $U(Y \rightarrow \pm\infty, Z, T) = 0$. From the thermal wind relation in Eq. (3) we obtain

$$U_g = -\frac{1}{f} e^{\alpha T} \int \frac{\partial B}{\partial Y} dZ. \quad (\text{A12})$$

Because the buoyancy anomaly ΔB [Eq. (A8)] and the vertical velocity W [Eqs. (A10a,b)] involve the vertical integral of alongfront velocity U , it is convenient to define a variable

$$\Phi(Y, Z, T) = \int_{-H}^Z U(Y, Z', T) dZ', \quad (\text{A13})$$

such that

$$U(Y, Z, T) = \frac{\partial}{\partial Z} \Phi(Y, Z, T), \quad (\text{A14})$$

$$B(Y, Z, T) = N^2 Z + B_0(Y) + \frac{N^2}{f} e^{\alpha T} \frac{\partial}{\partial Y} \Phi(Y, Z, T), \quad (\text{A15})$$

$$\Psi(Y, Z, T) = \frac{1}{f} \left(\alpha + \frac{\partial}{\partial T} \right) \Phi(Y, Z, T). \quad (\text{A16})$$

With the above definition of U and using Eqs. (A9) and (A12), Eq. (A3) becomes

$$\left[\left(\frac{\partial^2}{\partial T^2} + f^2 - \alpha^2 \right) \frac{\partial^2}{\partial Z^2} + N^2 e^{2\alpha T} \frac{\partial^2}{\partial Y^2} \right] \Phi = -f e^{\alpha T} \frac{dB_0}{dY}, \quad (\text{A17})$$

subject to boundary conditions $\Phi(Y \rightarrow \pm\infty, Z, T) = 0$ and $\Phi(Y, Z = -H, T) = \Phi(Y, Z = 0, T) = 0$ to enforce rigid lid conditions. One of the key assumptions in semigeostrophic theory is $D^2/DT^2 \ll f^2$, i.e., that the Lagrangian time scale of the flow is much larger than the inertial period (Hoskins 1975), and together with the weak strain limit $\alpha \ll f$, the above equation can be further simplified to

$$\left(f^2 \frac{\partial^2}{\partial Z^2} + N^2 e^{2\alpha T} \frac{\partial^2}{\partial Y^2} \right) \Phi = -f e^{\alpha T} \frac{dB_0}{dY}. \quad (\text{A18})$$

Equation (A18) describes the evolution of semigeostrophic frontogenesis. The solution of Φ can be written as the sum of vertical sine modes,

$$\Phi(Y, Z, T) = \sum_{n=1}^{\infty} \sin(m_n Z) \int_{-\infty}^{\infty} \hat{\Phi}(l, m_n, T) e^{ilY} dl, \quad (\text{A19})$$

where l and $m_n = n\pi/H$ are the horizontal and vertical wavenumbers, respectively, and a “hat” denotes the Fourier mode amplitude. Substituting Eq. (A19) into Eq. (8) we obtain

$$\hat{\Phi} = -\frac{ifle^{\alpha T} \widehat{B}_0 A_n}{f^2 + N^2 e^{2\alpha T} l^2 / m_n^2}, \quad (\text{A20})$$

with

$$A_n = \frac{2}{n\pi} [-1 + (-1)^n]. \quad (\text{A21})$$

Once the solution of $\Phi(Y, Z, T)$ is known, the other solutions of alongfront velocity $U(Y, Z, T)$, buoyancy field $B(Y, Z, T)$ and ASC streamfunction $\Psi(Y, Z, T)$ are obtained by using Eqs. (A14)–(A16), respectively.

APPENDIX B

Dimensional Quantities Used in the Numerical Simulations

The dimensional values of the simulation parameters are summarized in Table B1.

TABLE B1. Description and values of the simulation parameters.

Parameter	Definition	Value
L	Domain size in y direction	1000 km
H	Domain size in z direction	1 km
Λ	Cross-front length scale	200 km
n_y	Number of uniform grid points in y direction	3500
n_z	Number of uniform grid points in z direction	240
\mathcal{B}	Initial amplitude of the localized front	-0.06 m s^{-2}
N	Buoyancy frequency	10^{-2} s^{-1}
f	Coriolis frequency	10^{-4} s^{-1}
ν	Viscosity	$2 \times 10^{-4} \text{ m}^2 \text{ s}^{-1}$
κ	Diffusivity	$2 \times 10^{-4} \text{ m}^2 \text{ s}^{-1}$
ν_h	Hyerviscosity	$5 \times 10^7 \text{ m}^4 \text{ s}^{-1}$
κ_h	Hyperdiffusivity	$5 \times 10^7 \text{ m}^4 \text{ s}^{-1}$

APPENDIX C

Analytical Estimates for Energy Exchanges with High-Frequency IWs

We provide here analytical estimates for the dominant energy exchange terms between the mean flow and high-frequency IWs, the DSP and BFLUX (Fig. 12). As shown in Fig. 6, the high-frequency IW escapes the frontal region after about one inertial period. Consequently, the energy exchanges occur outside of the frontal zone where $S^2, \text{Ro} \rightarrow 0$. Equations (10a), (10b), (10d), therefore, simplify to

$$\frac{\partial u}{\partial t} - \alpha y \frac{\partial u}{\partial y} = -\alpha u + f v, \quad (\text{C1a})$$

$$\frac{\partial v}{\partial t} - \alpha y \frac{\partial v}{\partial y} = \alpha v - f u, \quad (\text{C1b})$$

$$\frac{\partial b}{\partial t} - \alpha y \frac{\partial b}{\partial y} + N^2 w = 0, \quad (\text{C1c})$$

with solutions of the form

$$u(y, z, t) = u_0(z) e^{-\alpha t} e^{i[l(t)y - \omega(t)t]}, \quad (\text{C2a})$$

$$v(y, z, t) = v_0(z) e^{\alpha t} e^{i[l(t)y - \omega(t)t]}, \quad (\text{C2b})$$

$$b(y, z, t) = b_0(z) e^{\alpha t} e^{i[l(t)y - \omega(t)t]}, \quad (\text{C2c})$$

where $u_0(z)$, $v_0(z)$ and $b_0(z)$ denote the initial modal structure of u , v and b , respectively. In this case, the imposed strain, α , acts to exponentially increase the horizontal wave-number like $l(t) = l_0 e^{\alpha t}$, where $l_0 = l(t=0)$ (Craik 1989; Thomas 2012). The corresponding IW frequency is

$$\omega(t) = f \sqrt{1 + \left[\frac{l(t)N}{fm} \right]^2}. \quad (\text{C3})$$

Plugging the solutions (C2a), (C2b) to the definition of DSP in Eq. (23) leads to

$$\text{DSP} = \alpha(v_0^2 e^{2\alpha t} - u_0^2 e^{-2\alpha t}), \quad (\text{C4})$$

which further simplifies to

$$\text{DSP} = \text{DSP}_0 + 4\alpha^2 t K_0, \quad (\text{C5a})$$

$$\int_0^t \text{DSP} dt \approx t \text{DSP}_0, \quad (\text{C5b})$$

in the limit $\alpha t \ll 1$. Above, $\text{DSP}_0 = \alpha(v_0^2 - u_0^2)$ and $K_0 = 1/2(v_0^2 + u_0^2)$. Equation (C5b) shows that the integrated $\langle \text{DSP} \rangle$ should increase linearly with time (thick blue line in Fig. C1). The solution of w can be obtained from continuity Eq. (10e), and is given by

$$w(y, z, t) = -ilw_0(z) e^{\alpha t} e^{i[l(t)y - \omega(t)t]}, \quad (\text{C6})$$

where $v_0 = m_n w_0$. From Eq. (C2c)

$$b_0(z) = il \frac{N^2(\alpha + i\omega)}{\alpha^2 + \omega^2} w_0(z) \approx il \frac{N^2(\alpha + i\omega)}{\omega^2} w_0(z), \quad (\text{C7})$$

because $\omega \gg \alpha$. Finally, the BFLUX takes the form

$$\text{BFLUX} \approx -\alpha \frac{N^2 l^2}{\omega^2} w_0^2. \quad (\text{C8})$$

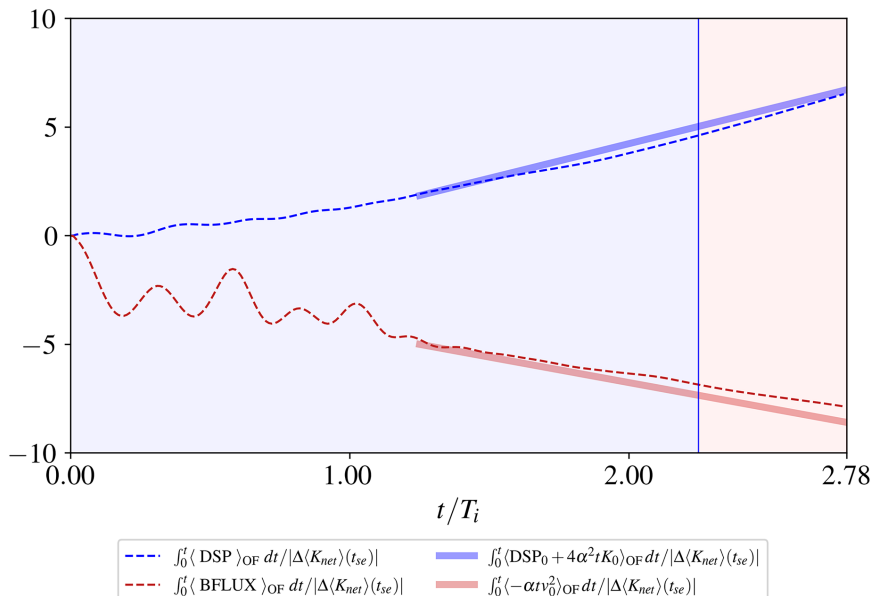


FIG. C1. As in Fig. 12b, but only the DSP and BFLUX terms are shown. Thick lines denote the theoretical estimates [Eqs. (C5a) and (C9b)] beginning at $t = 1.25T_i$ when the high frequency has largely escaped the frontal zone.

For a high-frequency IW ($\omega > f$) the dispersion relation simplifies to $\omega \approx Nl/m_n$ and Eq. (C8) becomes

$$\text{BFLUX} \approx -\alpha m_n^2 w_0^2 = -\alpha v_0^2, \quad (\text{C9a})$$

$$\int_0^t \text{BFLUX} dt \approx -\alpha t v_0^2. \quad (\text{C9b})$$

The above equations show that the BFLUX is a negative quantity that converts wave KE to wave PE. As time progresses, the imposed strain makes wave hodograph more rectilinear (i.e., $|v| \gg |u|$), leading to $\text{DSP} \approx \alpha v^2$ and to the asymptotic limit $\text{BFLUX} \rightarrow -\text{DSP}$ (thick brown line in Fig. C1).

REFERENCES

- Asselin, O., and W. R. Young, 2019: An improved model of near-inertial wave dynamics. *J. Fluid Mech.*, **876**, 428–448, <https://doi.org/10.1017/jfm.2019.557>.
- Barkan, R., K. B. Winters, and J. C. McWilliams, 2017: Stimulated imbalance and the enhancement of eddy kinetic energy dissipation by internal waves. *J. Phys. Oceanogr.*, **47**, 181–198, <https://doi.org/10.1175/JPO-D-16-0117.1>.
- , M. J. Molemaker, K. Srinivasan, J. C. McWilliams, and E. A. D’Asaro, 2019: The role of horizontal divergence in submesoscale frontogenesis. *J. Phys. Oceanogr.*, **49**, 1593–1618, <https://doi.org/10.1175/JPO-D-18-0162.1>.
- , K. Srinivasan, L. Yang, J. C. McWilliams, J. Gula, and C. Vic, 2021: Oceanic mesoscale eddy depletion catalyzed by internal waves. *Geophys. Res. Lett.*, **48**, e2021GL094376, <https://doi.org/10.1029/2021GL094376>.
- Burns, K. J., G. M. Vasil, J. S. Oishi, D. Lecoanet, and B. P. Brown, 2020: Dedalus: A flexible framework for numerical simulations with spectral methods. *Phys. Rev. Res.*, **2**, 023068, <https://doi.org/10.1103/PhysRevResearch.2.023068>.
- Capet, X., J. C. McWilliams, M. J. Molemaker, and A. Shchepetkin, 2008: Mesoscale to submesoscale transition in the California Current System. Part II: Frontal processes. *J. Phys. Oceanogr.*, **38**, 44–64, <https://doi.org/10.1175/2007JPO3672.1>.
- Craik, A., 1989: The stability of unbounded two-and three-dimensional flows subject to body forces: Some exact solutions. *J. Fluid Mech.*, **198**, 275–292, <https://doi.org/10.1017/S0022112089000133>.
- D’Asaro, E. A., and Coauthors, 2018: Ocean convergence and the dispersion of flotsam. *Proc. Natl. Acad. Sci. USA*, **115**, 1162–1167, <https://doi.org/10.1073/pnas.1718453115>.
- Dong, J., B. Fox-Kemper, H. Zhang, and C. Dong, 2021: The scale and activity of symmetric instability estimated from a global submesoscale-permitting ocean model. *J. Phys. Oceanogr.*, **51**, 1655–1670, <https://doi.org/10.1175/JPO-D-20-0159.1>.
- Eyink, G. L., 2005: Locality of turbulent cascades. *Physica D*, **207**, 91–116, <https://doi.org/10.1016/j.physd.2005.05.018>.
- Ferrari, R., and C. Wunsch, 2009: Ocean circulation kinetic energy: Reservoirs, sources, and sinks. *Annu. Rev. Fluid Mech.*, **41**, 253–282, <https://doi.org/10.1146/annurev.fluid.40.111406.102139>.
- Gerkema, T., and V. I. Shrira, 2005: Near-inertial waves in the ocean: Beyond the ‘traditional approximation.’ *J. Fluid Mech.*, **529**, 195–219, <https://doi.org/10.1017/S0022112005003411>.
- Gertz, A., and D. N. Straub, 2009: Near-inertial oscillations and the damping of midlatitude gyres: A modeling study. *J. Phys. Oceanogr.*, **39**, 2338–2350, <https://doi.org/10.1175/2009JPO4058.1>.
- Gula, J., M. J. Molemaker, and J. C. McWilliams, 2014: Submesoscale cold filaments in the Gulf Stream. *J. Phys. Oceanogr.*, **44**, 2617–2643, <https://doi.org/10.1175/JPO-D-14-0029.1>.
- Hoskins, B. J., 1975: The geostrophic momentum approximation and the semi-geostrophic equations. *J. Atmos. Sci.*, **32**, 233–242, [https://doi.org/10.1175/1520-0469\(1975\)032<0233:TGMAT>2.0.CO;2](https://doi.org/10.1175/1520-0469(1975)032<0233:TGMAT>2.0.CO;2).
- , 1982: The mathematical theory of frontogenesis. *Annu. Rev. Fluid Mech.*, **14**, 131–151, <https://doi.org/10.1146/annurev.fl.14.010182.001023>.
- , and F. P. Bretherton, 1972: Atmospheric frontogenesis models: Mathematical formulation and solution. *J. Atmos. Sci.*, **29**, 11–37, [https://doi.org/10.1175/1520-0469\(1972\)029<0011:AFMMFA>2.0.CO;2](https://doi.org/10.1175/1520-0469(1972)029<0011:AFMMFA>2.0.CO;2).
- Jing, Z., L. Wu, and X. Ma, 2017: Energy exchange between the mesoscale oceanic eddies and wind-forced near-inertial oscillations. *J. Phys. Oceanogr.*, **47**, 721–733, <https://doi.org/10.1175/JPO-D-16-0214.1>.
- Kunze, E., 1985: Near-inertial wave propagation in geostrophic shear. *J. Phys. Oceanogr.*, **15**, 544–565, [https://doi.org/10.1175/1520-0485\(1985\)015<0544:NIWPIG>2.0.CO;2](https://doi.org/10.1175/1520-0485(1985)015<0544:NIWPIG>2.0.CO;2).
- Large, W. G., J. C. McWilliams, and S. C. Doney, 1994: Oceanic vertical mixing: A review and a model with a nonlocal boundary layer parameterization. *Rev. Geophys.*, **32**, 363–403, <https://doi.org/10.1029/94RG01872>.
- McComas, C. H., and F. P. Bretherton, 1977: Resonant interaction of oceanic internal waves. *J. Geophys. Res.*, **82**, 1397–1412, <https://doi.org/10.1029/JC082i009p01397>.
- McWilliams, J. C., 2016: Submesoscale currents in the ocean. *Proc. Roy. Soc.*, **472A**, 20160117, <https://doi.org/10.1098/rspa.2016.0117>.
- Müller, P., J. C. McWilliams, and M. J. Molemaker, 2005: Routes to dissipation in the ocean: The 2D/3D turbulence conundrum. *Marine Turbulence*, H. B. J. Simpson and J. Sündermann, Eds., Cambridge University Press, 397–405.
- Munk, W., L. Armi, K. Fischer, and F. Zachariasen, 2000: Spirals on the sea. *Proc. Roy. Soc.*, **456A**, 1217–1280, <https://doi.org/10.1098/rspa.2000.0560>.
- Nagai, T., A. Tandon, E. Kunze, and A. Mahadevan, 2015: Spontaneous generation of near-inertial waves by the Kuroshio Front. *J. Phys. Oceanogr.*, **45**, 2381–2406, <https://doi.org/10.1175/JPO-D-14-0086.1>.
- Rocha, C. B., G. L. Wagner, and W. R. Young, 2018: Stimulated generation: Extraction of energy from balanced flow by near-inertial waves. *J. Fluid Mech.*, **847**, 417–451, <https://doi.org/10.1017/jfm.2018.308>.
- Salmon, R., 1980: Baroclinic instability and geostrophic turbulence. *Geophys. Astrophys. Fluid Dyn.*, **15**, 167–211, <https://doi.org/10.1080/03901928008241178>.
- Shakespeare, C. J., and J. R. Taylor, 2013: A generalized mathematical model of geostrophic adjustment and frontogenesis: Uniform potential vorticity. *J. Fluid Mech.*, **736**, 366–413, <https://doi.org/10.1017/jfm.2013.526>.
- Srinivasan, K., R. Barkan, and J. C. McWilliams, 2022: A forward energy flux at submesoscales driven by frontogenesis. *J. Phys. Oceanogr.*, **53**, 287–305, <https://doi.org/10.1175/JPO-D-22-0001.1>.
- Taylor, S., and D. Straub, 2016: Forced near-inertial motion and dissipation of low-frequency kinetic energy in a wind-driven channel flow. *J. Phys. Oceanogr.*, **46**, 79–93, <https://doi.org/10.1175/JPO-D-15-0060.1>.

- Thomas, L. N., 2012: On the effects of frontogenetic strain on symmetric instability and inertia–gravity waves. *J. Fluid Mech.*, **711**, 620–640, <https://doi.org/10.1017/jfm.2012.416>.
- , 2019: Enhanced radiation of near-inertial energy by frontal vertical circulations. *J. Phys. Oceanogr.*, **49**, 2407–2421, <https://doi.org/10.1175/JPO-D-19-0027.1>.
- Thomas, J., and S. Arun, 2020: Near-inertial waves and geostrophic turbulence. *Phys. Rev. Fluids*, **5**, 014801, <https://doi.org/10.1103/PhysRevFluids.5.014801>.
- , and D. Daniel, 2021: Forward flux and enhanced dissipation of geostrophic balanced energy. *J. Fluid Mech.*, **911**, A60, <https://doi.org/10.1017/jfm.2020.1026>.
- Thomas, L. N., and C. M. Lee, 2005: Intensification of ocean fronts by down-front winds. *J. Phys. Oceanogr.*, **35**, 1086–1102, <https://doi.org/10.1175/JPO2737.1>.
- , A. Tandon, and A. Mahadevan, 2008: Submesoscale processes and dynamics. *Ocean Modeling in an Eddying Regime, Geophys. Monogr.*, Vol. 177, Amer. Geophys. Union, 17–38.
- Wagner, G., and W. Young, 2016: A three-component model for the coupled evolution of near-inertial waves, quasi-geostrophic flow and the near-inertial second harmonic. *J. Fluid Mech.*, **802**, 806–837, <https://doi.org/10.1017/jfm.2016.487>.
- Weller, R. A., 1982: The relation of near-inertial motions observed in the mixed layer during the Jas in (1978) experiment to the local wind stress and to the quasi-geostrophic flow field. *J. Phys. Oceanogr.*, **12**, 1122–1136, [https://doi.org/10.1175/1520-0485\(1982\)012<1122:TRONIM>2.0.CO;2](https://doi.org/10.1175/1520-0485(1982)012<1122:TRONIM>2.0.CO;2).
- Whitt, D. B., and L. N. Thomas, 2013: Near-inertial waves in strongly baroclinic currents. *J. Phys. Oceanogr.*, **43**, 706–725, <https://doi.org/10.1175/JPO-D-12-0132.1>.
- , and —, 2015: Resonant generation and energetics of wind-forced near-inertial motions in a geostrophic flow. *J. Phys. Oceanogr.*, **45**, 181–208, <https://doi.org/10.1175/JPO-D-14-0168.1>.
- Xie, J.-H., 2020: Downscale transfer of quasigeostrophic energy catalyzed by near-inertial waves. *J. Fluid Mech.*, **904**, A40, <https://doi.org/10.1017/jfm.2020.709>.
- , and J. Vanneste, 2015: A generalised-lagrangian-mean model of the interactions between near-inertial waves and mean flow. *J. Fluid Mech.*, **774**, 143–169, <https://doi.org/10.1017/jfm.2015.251>.
- Young, W., and M. Ben Jelloul, 1997: Propagation of near-inertial oscillations through a geostrophic flow. *J. Mar. Res.*, **55**, 735–766.
- Yu, X., A. C. Naveira Garabato, A. P. Martin, D. Gwyn Evans, and Z. Su, 2019: Wind-forced symmetric instability at a transient mid-ocean front. *Geophys. Res. Lett.*, **46**, 11 281–11 291, <https://doi.org/10.1029/2019GL084309>.